








Article

Sulfosalts and Sulfates in the Epithermal Au-Ag-Te Emmy Deposit (Khabarovsk Territory, Far East of Russia): Implications for the Mineralization Process

Tamara Yu. Yakich ^{1,*} , Panagiotis Voudouris ² , Darya V. Levochskaia ³, Alexey K. Mazurov ¹, Mikhail V. Shaldybin ^{1,4} , Yuriy M. Lopushnyak ⁵, Alexey S. Ruban ¹ , Evan Dasi ¹ , Prokopi N. Maximov ¹ , Ekaterina A. Sinkina ¹, Ksenia V. Bestemianova ⁶ and Maxim A. Rudmin ¹ 

¹ School of Earth Sciences & Engineering, Division for Geology, Tomsk Polytechnic University, 634050 Tomsk, Russia; akm@tpu.ru (A.K.M.); shaldybinmv@yandex.ru (M.V.S.); ruban@tpu.ru (A.S.R.); de01@tpu.ru (E.D.); pnm1@tpu.ru (P.N.M.); vea@tpu.ru (E.A.S.); rudminma@tpu.ru (M.A.R.)

² Faculty of Geology and Geoenvironment, National and Kapodistrian University of Athens, Zografou, GR-15784 Athens, Greece; voudouris@geol.uoa.gr

³ Khabarovsk Branch of JSC “Polymetal UK”, 680000 Khabarovsk, Russia; levochskayadv@polymetal.ru

⁴ JSC “TomskNIPIneft”, 634027 Tomsk, Russia

⁵ LLC “NPP Qualitet”, 140000 Moscow, Russia; lum83@mail.ru

⁶ Laboratory of Geochronology and Geodynamics, Department of Geology and Geography, Tomsk State University, 634050 Tomsk, Russia; ksenijavt@mail.ru

* Correspondence: cherkasovatu@tpu.ru

Abstract: This study considers the features of the chemical composition, internal structure, and oscillatory zoning of sulfosalts and sulfates in the epithermal high–intermediate-sulfidation-type Au-Ag-Te Emmy deposit (Khabarovsk Territory, Russia). In Emmy deposit, sulfosalts primarily represent goldfieldite, probably corresponding to a high-sulfidation (HS) mineral association replaced by tennantite–tetrahedrite group minerals. The latter is associated with tellurides and native tellurium, corresponding to an intermediate-sulfidation (IS)-type ore assemblage and suggesting an increasing influx of Te, Sb, and As in the system. Goldfieldite is replaced by native tellurium and tellurides along its growth zones, and is characterized by oscillatory zoning. The replacement of goldfieldite by mercury, nickel, lead, and copper tellurides indicate a new influx of native gold, native tellurium, and gold–silver tellurides into the open mineral-forming system. At deeper levels of the Emmy deposit, an advanced argillic alteration assemblage includes aluminum phosphate–sulfate (APS) minerals, represented by members of the svanbergite–woodhouseite series. Element mapping of the studied APS mineral grains indicated three distinct areas recording the evolution of the hydrothermal system in the Emmy: an oscillatory-zoned margin enriched in sulfur, lead, and barium, corresponding to the late influx of IS state fluids related to gold and tellurides; an intermediate part, which is leached and corresponds to the HS mineralization stage; and the central part of the grains, which is enriched in cerium, calcium, and strontium, resulting from a replacement of magmatic apatite in the pre-ore alteration stage. The leached zone between the core and rim of the APS grains is related to a change in crystallization conditions, possibly due to the mixing processes of the fluids with meteoric water. Barite, found in the upper level of the advanced argillic hypogene alteration assemblage, is also characterized by oscillatory zoning, associated with the enrichment of individual zones in lead. Micron gold particles associated with barite are confined to their lead-enriched zones. The study of fluid inclusions in quartz within the Emmy deposit showed the hydrothermal ore process at a temperature of 236–337 °C. Homogenization temperatures for quartz–pyrite–goldfieldite mineral association vary within 337–310 °C and salinity varies within 0–0.18 wt.%NaCl equivalent, and for gold–silver–telluride–polymetallic mineral association, they decrease and vary within 275–236 °C and salinity slightly increases from



Received: 13 November 2024

Revised: 8 January 2025

Accepted: 9 January 2025

Published: 14 January 2025

Citation: Yakich, T.Y.; Voudouris, P.; Levochskaia, D.V.; Mazurov, A.K.; Shaldybin, M.V.; Lopushnyak, Y.M.; Ruban, A.S.; Dasi, E.; Maximov, P.N.; Sinkina, E.A.; et al. Sulfosalts and Sulfates in the Epithermal Au-Ag-Te Emmy Deposit (Khabarovsk Territory, Far East of Russia): Implications for the Mineralization Process.

Geosciences **2025**, *15*, 26. <https://doi.org/10.3390/geosciences15010026>

Copyright: © 2025 by the authors. Licensee MDPI, Basel, Switzerland. This article is an open access article distributed under the terms and conditions of the Creative Commons Attribution (CC BY) license (<https://creativecommons.org/licenses/by/4.0/>).

0.18 to 0.35 wt.%NaCl equivalent. This study demonstrates that the nature of oscillatory zoning in sulfosalts and sulfates in the Emmy deposit results from an external process. Such a process is of fundamental importance from a genetic point of view.

Keywords: epithermal Au-Ag-Te Emmy deposit; Far East; oscillatory zoning; sulfosalts; aluminum phosphate–sulfate (APS) minerals

1. Introduction

Epithermal gold deposits are low-temperature deposits (<than 300 °C), usually located at depths of up to 1000 m [1], often accompanied by advanced argillic and silicic alteration [1–3]. In Russia, such deposits are widespread within the Far East, including both recent [4] and ancient (Cretaceous age) [5] Pacific Rim epithermal deposits. This type of ore deposit has recently become increasingly significant in Russia. However, it was previously not considered a gold source due to the complexity of enrichment and the small size of gold particles. In addition to gold and silver, these deposits contain many valuable metals/metalloids such as Te, As, Bi, Se, and Sb (TABSS), which are trace elements in another geological setting. Moreover, the established relationship between the critical TABSS elements and precious metals can be used as a sensitive indicator of the conditions for the formation of epithermal deposits and mineralization processes. TABSS elements can form their mineral phases and incorporate as trace elements in significant sulfides and sulfosalts, demonstrating fluid fluctuations during ore deposition and the various stages of ore concentration.

Minerals that host trace TABSS elements can act as markers of changes in physico-chemical conditions (redox potential, pH, or fluid parameters, for example, or sulfidation–oxidation reactions at redox fronts) [6,7]. Sulfides, sulfosalts, and tellurides are particularly interesting, as they accompany precious metals in ore deposits [6–10]. For example, gold and silver tellurides themselves can constitute a significant proportion of the total gold budget in a deposit [11]. Examples of these deposits include the following: Cripple Creek and Golden Sunlight gold–silver–telluride deposits in the U.S.A. (Montana) [12], Emperor deposit (Fiji) [13], Dongping gold deposit (Hebei Province, China) [14], Acupan and Baguio gold–silver–telluride districts (Philippines) [15], Sacarimb deposit (Romania) [16], Kochbulak gold–telluride deposit (Uzbekistan) [17,18], Perama Hill Au-Ag-Te-Se deposit (Greece) [19], Maletoyvayam deposit (Koryak Highland, Russia) [20,21], and Emmy gold–silver–telluride deposit (Khabarovsk Territory, Russia) ([22], this study). The formation of such deposits has been associated with deposition from fluids rich in TABSS elements formed under certain regional conditions, for example, due to the subduction of tellurium-rich sediments of the ocean floor, as observed within the Pacific Rim.

Bulk ore data of precious metal-bearing epithermal deposits provide little genetic information about the sources, transport modes, fluctuations of the ore-bearing solution, and the process of mineralization. The features of the mineral–chemical composition, crystal habit, and internal structure of accompanying minerals can be more informative. For example, oscillatory zoning—periodically repeating the maxima and minima of the values of any component, as a process of organization of matter in the process of hydrothermal mineral formation—is often encountered [23–26]. The factors that control the oscillatory zoning of minerals can be both internal (i.e., self-organization mechanisms), due to the ability of a crystal to absorb one or another component to varying degrees (such zoning is individual for each crystal), or external (general); as a rule, the nature of zoning is preserved in different grains and the number of bands in adjacent crystals is the same [24–26]. The

last type of zoning is informative, as it may indicate any periodic changes in the mineral-forming environment. According to Holten et al. [25], oscillatory mineral zonation is usually associated with crystal growth in an open system, and is characterized by non-equilibrium states. The zonation patterns will result in coupling between the generally nonlinear crystal growth dynamics and the boundary conditions imposed by externally controlled fluctuations [25].

This study expands on previous work by Yakich et al. [22] on the Svetloye epithermal district within the Okhotsk–Chukotka volcanic belt. It presents new data on sulfosalt and sulfate mineralogy of the Emmy deposit in this field. Emphasis is placed upon oscillatory-zoned minerals in the deposit, namely goldfieldite (a member of the tetrahedrite group [27]), aluminum phosphate–sulfate (APS) minerals (members of the alunite supergroup of minerals) [28–32]), and barite, which form part of the advanced argillic alteration assemblage and are described here for the first time from the deposit. We use oscillatory zoning and fluid microthermometry in quartz as tools for decoding the genetic information contained in sulfosalts and sulfate crystals, aiming to reconstruct the conditions of deposit formation.

2. Geological Background

2.1. Geology of the Emmy Deposit

The gold–silver telluride Emmy deposit is part of the Svetloye epithermal gold ore district, which, in turn, is confined to the Ul'insky trough, composed of Cretaceous volcanic formations of the Okhotsk–Chukotka volcanic belt [33]. The Svetloye ore district contains several deposits: Emmy, Lyudmila, Elena, Tamara, and Larisa [22]. The Emmy deposit is confined to the northwestern volcanic edifice from the Coniacian–Santonian age (K_2). It differs from all the other deposits in the Svetloye ore district due to the presence of abundant telluride mineralization not found in the other deposits and confined to the southeastern volcanic center (Elena, Tamara, Lyudmila, and Larisa deposits). The latter is hosted within the dacite–rhyolite–leucogranite formation of the Urak suite (Campanian–Maastrichtian time age (K_2)). The Khetanian Suite hosting the Emmy deposit is represented by andesites, basaltic andesites, their agglomerate lavas, and more rarely, tuffs [22].

2.2. Mineralogy and Petrography of Altered Rocks

Based on the results of mineralogical and petrographic studies of 120 hand specimens and their thin sections and using the interpretation of ASTER (Advanced Spaceborne Thermal Emission and Reflection Radiometer) data [34], a schematic map and cross-section of hydrothermal alteration mineral zones for the Emmy deposit were developed (Figure 1a,b). It was established that within the Emmy deposit, the wall rock alteration of the host rocks is mainly represented by residual quartz and brecciated residual quartz (Figure 1c,d) and to a lesser extent alunite- and dickite-bearing advanced argillic alteration (Figure 1e,f) as well as quartz–muscovite-altered rocks (Figure 1g). In the latter alteration zone, the primary host andesitic rocks and their tuffs display various degrees of alteration, with the relict outlines of porphyritic phenocrysts replaced by sericite, muscovite, or illite (Figure 1h) [5].

Residual quartz zone: The groundmass of the rocks is composed of allotriomorphic, granular (0.01–0.02 mm in size) quartz (I) of the metasomatic stage, among which larger quartz (IIb and III) grains (up to 1 mm) are observed. The rock is characterized by many differently oriented, mutually intersecting fractures (Figure 1c; hand specimen No. 1). The fractures are filled with euhedral quartz (III), forming a system of intersecting veinlets. It is also found that open spaces and druses are common (up to 4 mm) in the altered rocks.

Three generations of quartz have been distinguished: (i) is allotriomorphic, micro-, and, less often, fine-grained quartz, which makes up the bulk of the rock (Qz I); (ii) is (a) fine-grained or moganite quartz, growing along fractures (IIa) and (b) comb well-

crystallized quartz, filling fractures and vugs (IIb), and overgrown quartz II, forming clusters up to 2 mm (III) in diameter in the groundmass of the rock, and (iii) accompanied by tellurides. The silicified rock is characterized by a high content of opaque minerals (more than 5 vol. %), represented by pyrite. Opaque minerals form linear (Figure 1c,f) and cluster-like assemblages (Figure 1d) and sporadic grains regularly dispersed in the groundmass.

The residual vuggy quartz zone is the most abundant and common rock type compared to other structural and textural rock varieties occurring within the Emmy deposit. The size of the vugs varies from 0.05 to 2 mm (average 0.2 mm), with vugs covering up to 50% of the total volume of the thin section area. The vugs are characterized by overgrowth textures, which are characterized by the development of euhedral quartz (IIb and III) along the walls of the vugs (Figure 1c).

The brecciated residual quartz zone is represented by quartz I developing in silicified volcanic rock matrix cementing clasts. Comb quartz (IIb and III) is observed, which overgrows large cavities (Figure 1d). The groundmass of the silicified rock fragments is composed of allotriomorphic, granular quartz I (0.01–0.03 mm) with disseminated pyrite I. Quartz in the silicified fragments is fractured and crosscut by quartz II–pyrite II veinlets. Pyrite dissemination has a streaky mass character. Pyrite is brecciated and associated with prismatic rutile crystals.

The quartz–alunite zone is characterized by a porphyroblastic texture (Figure 1e). The rock comprises a dark brown microcrystalline quartz I–clay aggregate fractured by fractures up to 1 mm wide (Figure 1e). The fractures are filled with coarse-grained alunite represented by long prismatic crystals of up to 0.01 mm in size. In addition to filling fractures, alunite forms monomineralic clustered aggregates with a diameter of up to 1 mm. Alunite has needle-shaped crystals of up to 0.2 mm in size in these clusters. APS (aluminum phosphate–sulfate) minerals are not found in this zone, but barite may occur.

The quartz–dickite–kaolinite zone is composed of fine-grained quartz I (0.01–0.05 mm) of an allotriomorphic texture associated with fine dickite/kaolinite flakes, among which larger grains of quartz II (up to 0.5 mm) are distinguished. The content of dickite/kaolinite is about 15 vol.% of the section area. In the groundmass, there are zones with crystals of euhedral quartz III, having a zonal structure and ranging in size from 0.5 to 1 mm, with cavities between crystals of up to 2 mm. Quartz III aggregates have a mosaic block structure. This zone is associated with ore mineralization, represented by pyrite II deposited from the first ore phase, which can form elongated zones (Figure 2f). In this zone, APS minerals are present at a depth of 130–150 m from the top drill hole Em 3 (Figure 1b, APS sampling point is marked with an asterisk).

Quartz–muscovite zones are found as interlayers between residual vuggy quartz and quartz–dickite zones. This zone is observed in shallow levels (Figure 1b,g) and at a depth of about 100–120 m within the drill hole Em 3. In the intergranular space, the development of clay minerals such as kaolinite/dickite and pyrophyllite (at depth) are observed. The groundmass of the rock is composed of allotriomorphic, granular (0.01–0.02 mm) quartz I. Fan-shaped aggregates of muscovite/illite crystals stand out among the quartz II–clay aggregate (Figure 1g). The groundmass contains numerous vugs ~ 0.5 mm in diameter. Comb, euhedral quartz III (overgrowth textures) develops along the walls of the vugs up to the complete filling. The rock is crosscut by numerous fractures up to 2 mm wide, with an average thickness of 0.5 mm. The fractures are filled with quartz III (grain sizes up to 1 mm), muscovite/illite (up to 0.5 mm), and metallic minerals. Ore mineralization occurs in veinlets and disseminations uniformly dispersed in the groundmass (Figure 1g). The grain sizes of metallic minerals do not exceed 0.02 mm.

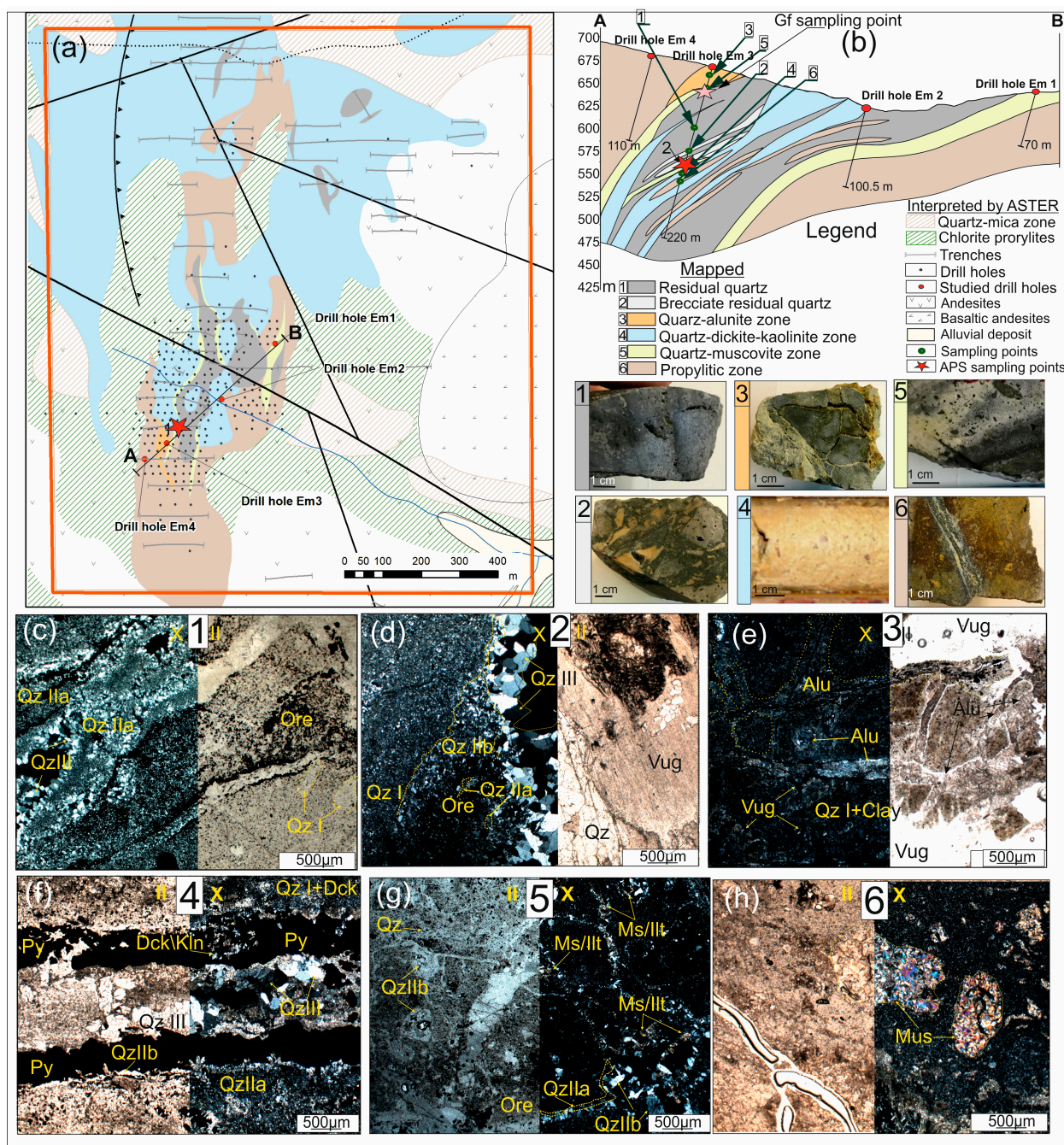


Figure 1. (a) Schematic map of hydrothermal alteration zones and (b) geological cross-section (AB) of the Emmy deposit, according to the author's data (hand specimens (1–6) and thin sections (c–h)), and data obtained from ASTER images [34]. Photographs of hand specimens and transmitted light microphotographs of thin sections in plane (II)- and cross (X)-polarized light of the main varieties of altered rocks. (c) Residual vuggy quartz zone with colloform (IIa) and comb quartz (Qz III) filling vugs, and dissemination of ore minerals (Ore). (d) Brecciated residual quartz zone with rock fragments composed of groundmass of allotriomorphic, fine-grained microgranular quartz (Qz I) and unevenly distributed ore dissemination (Ore). Zoned crystals of colloform (IIa) and euhedral quartz (Qz IIb, III) overgrow cavities (Vug). (e) Quartz-alunite zone with alunite (Alu) in veinlets and also filling voids (Vug) of the quartz (Qz I). (f) Quartz-dickite-kaolinite zone composed of fine-grained quartz (Qz I) and dickite/kaolinite (Dck/Kln) with Pyrite (Py I) of first ore phase associated with colloform (QzIIa) comb quartz (QzIIb). (g) Quartz (QzIIa-IIb)-muscovite (Ms/Ilt)-altered rock with disseminated pyrite (IIb) with other metallic minerals (Ore) and muscovite/illite-quartz veinlets. (h) Muscovite-altered andesite with relic plagioclase phenocrysts replaced by muscovite (Ms) into quartz-altered groundmass.

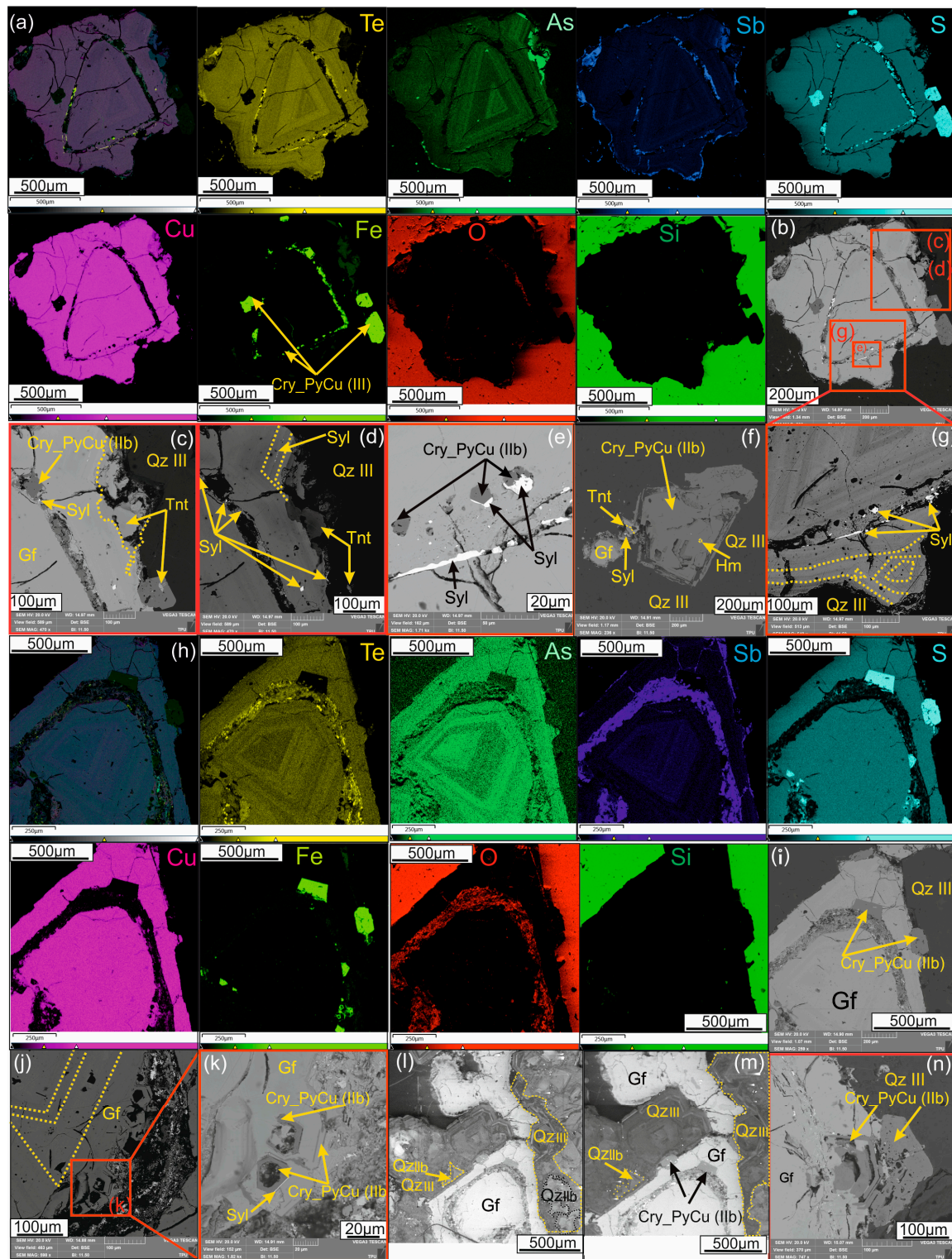


Figure 2. (a–k,n) Photomicrographs (SEM-BSE-SE images) with X-ray element mapping with distribution of Te, As, Sb, S, Cu, Fe, O, and Si, demonstrating goldfieldite (Gf) grains with oscillatory zonation in association with euhedral quartz (QzIIb and Qz III) replaced by tennantite (Tnt); (a–d,f) crystalline Cu-bearing pyrite (Cry_PyCu(IIb)) overgrowing with sylvanite (Syl); (c–e,g–k) confined to growth zones (i.e., zones of selective replacement of goldfieldite). Hemusite (Hm) is also present as a synchronous growth phase with crystalline Cu-bearing pyrite (Cry_PyCu(IIb)); (l,m) cathodoluminescence images demonstrating oscillatory-zoned quartz IIb in association with goldfieldite and quartz III overgrowing with goldfieldite and quartz IIb.

This zone contains APS minerals. They occur in a drill hole not shown in the cross-section at a depth of 117.8 m from the drill head (Figure 1b). Their location is marked with an asterisk No.1 only on the map (Figure 1a).

3. Samples and Methods

A total of 120 samples of altered rocks and ores were collected from four drill holes and surface outcrops in the Emmy deposit. Electronic and optical microscopy studied 50 polished blocks and 120 thin sections of samples from mineralized veins and alteration zones. Suitable thin sections and polished sections were selected for the study of major and trace element analyses and mineral detection. Backscattered electron (BSE) images were taken using a Tescan Vega 3 SBU scanning electron microscope equipped with an energy dispersive spectrometer (EDS) from Oxford Instruments (Tomsk city, Tomsk Polytechnic University, Russia), with an Aztec-based system of microanalysis and Tescan Vega 2 LMU scanning electron microscope combined with Oxford Instruments' INCA Energy 350 energy dispersive spectrometer and cathodoluminescence (CL) detector (Tomsk city, Tomsk State University, Russia). The operating conditions were in the high vacuum mode ($<9 \times 10^{-3}$ Pa) at an accelerating voltage of 20 kV, with a high resolution and a distance of 15 mm. The measurement parameters of accelerating voltage were 10–20 kV, beam current 1.2–3.5 nA, and beam size 180–500 nm. The EDS detector was calibrated using Co standard K-series 10.0063 eV, peak area 350,050. Samples containing APS were analyzed using powder X-ray diffraction of bulk samples. XRD patterns were recorded using a Rigaku Ultima IV X-ray diffractometer with a Cu anode, an X-ray tube voltage of 40 kV, a current of 30 mA, and a power of 1.2 kW. Whole rock samples were scanned from 5 to 60° 2 θ at a scanning speed of 1° per minute with a step of 0.02°. In addition to the bulk samples, clay fractions were also separated by sedimentation following disaggregation and dispersion. In order to fully characterize the clay minerals, the clay fractions were scanned in the air-dried state, then after saturation with glycol overnight and after heat treatment at 550 °C for 1 h. Comprehensive identification of the clay minerals was conducted following procedures given by Moore and Reynolds [35]. Quantitative mineralogical analyses of the whole rock data were performed by a Rietveld analysis [36], using PDXL and Siroquant software [37]. We have conducted fluid microthermometry on twenty doubly polished thick sections of quartz. Microthermometric measurements were performed by the Linkam THGM 600 freezing–heating stage mounted on an Axio Scope. A1 microscope. The precision of the temperature measurements was ± 0.5 °C for heating and ± 0.2 °C for freezing. Salinities, pressure, and densities of fluid inclusions were calculated using HokieFlinco H₂O–NaCl (a Microsoft Excel spreadsheet for interpreting microthermometric data from fluid inclusions based on the PVTX properties of H₂O–NaCl) [38]. A confocal Thermo Fisher Scientific DXR2 Raman spectrometer was used to identify the inclusions' vapor and liquid composition. All measurements were carried out with a laser wavelength of 785 nm and 20–25 mW power. Spectra were acquired over a 5 s period for 0–3.364 cm^{−1} with a three-rate accumulation. Calibration stability of the thermal stage was controlled by the melting temperature of carbon dioxide in an artificial/reference inclusion H₂O–CO₂ in quartz. All microthermometry and Raman spectroscopy analyses were carried out in the laboratory of Tomsk Polytechnic University, Russia.

4. Results

4.1. Sulfosalts

The Emmy deposit develops a variety of sulfosalts including tennantite–tetrahedrite [27] (Table 1, Supplementary Materials); bournonite, due to the galena's replacement; and emplectite, which appears in the form of single micron-sized grains in pyrite [22].

Table 1. Representative electron probe microanalyses of TGM from the Emmy deposit (Drill hole Em 3). Data normalized to 100% (bd: below detection).

Depth, m	Cu	Fe	Ag	Zn	Sb	As	Bi	Te	S	Total	Formula:
Tetrahedrite											
31.6	36.22	6.10	1.16	1.87	21.44	6.27	bd	bd	26.94	100.00	(Cu _{9.09} Ag _{0.17} Fe _{1.74} Zn _{0.46}) Σ _{11.46} (Sb _{2.81} As _{1.33}) Σ _{4.14} S _{13.4}
49.8	42.04	6.90	bd	bd	10.51	13.16	bd	bd	27.39	100.00	(Cu _{10.09} Fe _{1.88}) Σ _{11.97} (As _{2.68} Sb _{1.32}) Σ _{4.00} S _{13.03}
62.0	40.04	1.46	bd	3.94	21.83	2.19	bd	4.99	25.55	100.00	(Cu _{10.38} Zn _{0.99} Fe _{0.43}) Σ _{11.80} (Sb _{2.95} Te _{0.64} As _{0.48}) Σ _{4.08} S _{13.12}
76.2	37.88	6.63	bd	bd	26.00	3.18	bd	bd	26.32	100.00	(Cu _{9.65} Fe _{1.92}) Σ _{11.57} (Sb _{3.46} As _{0.69}) Σ _{4.14} S _{13.29}
83.2	37.27	6.54	bd	0.7	27.93	1.73	bd	bd	25.83	100.00	(Cu _{9.60} Fe _{1.92} Zn _{0.18}) Σ _{11.69} (Sb _{3.75} As _{0.38}) Σ _{4.13} S _{13.18}
109.8	35.74	9.04	bd	bd	26.45	2.24	bd	bd	26.54	100.00	(Cu _{9.07} Fe _{2.61}) Σ _{11.67} (Sb _{3.50} As _{0.48}) Σ _{3.98} S _{13.34}
Tennantite											
46.4	40.92	7.29	bd	bd	5.31	16.58	bd	bd	27.77	100.00	(Cu _{9.80} Fe _{1.99}) Σ _{11.97} (As _{3.37} Sb _{0.66}) Σ _{4.03} S _{13.18}
49.8	41.20	6.83	bd	bd	12.48	11.66	bd	0.64	27.19	100.00	(Cu _{9.99} Fe _{1.89}) Σ _{11.88} (As _{2.40} Sb _{1.58} Te _{0.08}) Σ _{4.06} S _{13.07}
70.2	38.49	8.68	bd	bd	11.16	13.85	bd	bd	27.82	100.00	(Cu _{9.22} Fe _{2.37}) Σ _{11.58} (As _{2.81} Sb _{1.40}) Σ _{4.21} S _{13.21}
76.2	41.99	7.59	bd	bd	0.84	20.47	bd	bd	29.11	100.00	(Cu _{9.66} Fe _{1.99}) Σ _{11.64} (As _{3.99} Sb _{0.1}) Σ _{4.09} S _{13.27}
83.2	42.21	7.64	bd	bd	1.02	20.36	bd	bd	28.76	100.00	(Cu _{9.74} Fe _{2.01}) Σ _{11.74} (As _{3.98} Sb _{0.12}) Σ _{4.11} S _{13.15}
Argentotetrahedrite											
31.6	4.11	5.16	47.12	1.99	14.47	6.11	-	-	21.05	100.00	(Ag _{8.55} Cu _{1.27} Fe _{1.81} Zn _{0.60}) Σ _{12.22} (Sb _{2.33} As _{1.60}) Σ _{3.92} S _{12.85}
Goldfieldite											
38.2	42.25	1.60	2.39	bd	6.11	3.12	bd	19.00	25.52	100.00	(Cu _{11.00} Ag _{0.37} Fe _{0.47}) Σ _{11.84} (Te _{2.46} Sb _{0.83} As _{0.69}) Σ _{3.98} S _{13.17}
38.8	44.93	bd	bd	bd	9.19	2.83	3.01	15.44	24.60	100.00	Cu _{11.90} (Te _{2.04} Sb _{1.27} As _{0.64} Bi _{0.24}) Σ _{11.90} S _{12.91}
38.2	44.16	bd	bd	bd	6.97	4.17	2.43	16.95	25.32	100.00	(Cu _{11.57}) Σ _{11.57} (Te _{2.21} Sb _{0.95} As _{0.93} Bi _{0.19}) Σ _{4.28} S _{13.15}
38.2	43.84	bd	bd	bd	7.39	3.42	2.38	17.80	25.17	100.00	(Cu _{11.55}) Σ _{11.55} (Te _{2.34} Sb _{1.02} As _{0.76} Bi _{0.19}) Σ _{4.31} S _{13.14}
38.2	44.91	0.61	bd	bd	8.04	3.16	bd	17.55	25.73	100.00	(Cu _{11.61} Fe _{0.18}) Σ _{11.79} (Te _{2.26} Sb _{1.08} As _{0.69} Bi _{0.19}) Σ _{4.04} S _{13.18}
38.2	44.07	bd	bd	bd	4.88	5.88	bd	19.03	26.13	100.00	(Cu _{11.32}) Σ _{11.32} (Te _{2.44} Sb _{0.65} As _{1.28}) Σ _{4.37} S _{13.31}
38.2	46.08	0.37	bd	bd	6.85	2.42	bd	19.08	25.19	100.00	(Cu _{11.98} Fe _{0.11}) Σ _{12.09} (Te _{2.47} Sb _{0.93} As _{0.53}) Σ _{3.93} S _{12.98}
38.2	43.00	1.40	bd	bd	5.58	2.84	bd	20.84	26.33	100.00	(Cu _{11.09} Fe _{0.41}) Σ _{11.50} (Te _{2.68} Sb _{0.75} As _{0.62}) Σ _{4.05} S _{13.45}
38.2	43.54	0.35	bd	bd	6.85	4.06	3.05	16.79	25.37	100.00	(Cu _{11.42} Fe _{0.10}) Σ _{11.53} (Te _{2.19} Sb _{0.94} As _{0.90} Bi _{0.24}) Σ _{4.28} S _{13.19}
38.2	46.09	0.91	bd	bd	8.34	2.89	bd	16.24	25.54	100.00	(Cu _{11.87} Fe _{0.27}) Σ _{12.13} (Te _{2.08} Sb _{1.12} As _{0.63}) Σ _{3.83} S _{13.03}
Stibiofieldite											
62.0	43.02	0.38	bd	0.80	14.30	1.98	1.98	12.23	25.32	100.00	(Cu _{11.32} Zn _{0.21} Fe _{0.11}) Σ _{11.64} (Sb _{1.96} Te _{1.60} As _{0.44} Bi _{0.16}) Σ _{4.16} S _{13.20}
38.2	43.85	0.86	bd	0.00	12.79	4.13	bd	12.62	25.75	100.00	(Cu _{11.32} Fe _{0.25}) Σ _{11.57} (Sb _{1.72} Te _{1.62} As _{0.91}) Σ _{4.25} S _{13.18}

In the Emmy deposit, goldfieldite and stibiofieldite were detected (Table 1). Goldfieldite contains later sylvanite, coloradoite, altaite, tellurantimony, tellurobismuthite, and melonite (Supplementary Materials) replacing goldfieldite along their growth zones. Goldfieldite in the Emmy deposit is characterized by oscillatory zoning, reflecting the different distributions of arsenic, antimony, and tellurium and the incorporation of bismuth in some places within the crystal structure (Figure 2, Table 1, Supplementary Figure S1).

After conducting cathodoluminescence analysis of euhedral quartz (IIb), which is associated with goldfieldite, and quartz (III) overgrowing quartz (IIb), it was found that both quartz's generations are characterized by oscillatory zoning (Figure 2l,m), indicating non-equilibrium conditions for the formation of these crystals.

4.2. APS Minerals

In the quartz–dickite–kaolinite and quartz–muscovite zones, the APS minerals are disseminated in an argillaceous substrate made up of hypogene kaolinite/dickite, pyrophyllite, muscovite, and quartz. The varieties, composition, and quantities of clay minerals accompanying APS minerals in the bulk rock are shown in the X-ray diffraction (XRD) pattern of Figure 3.

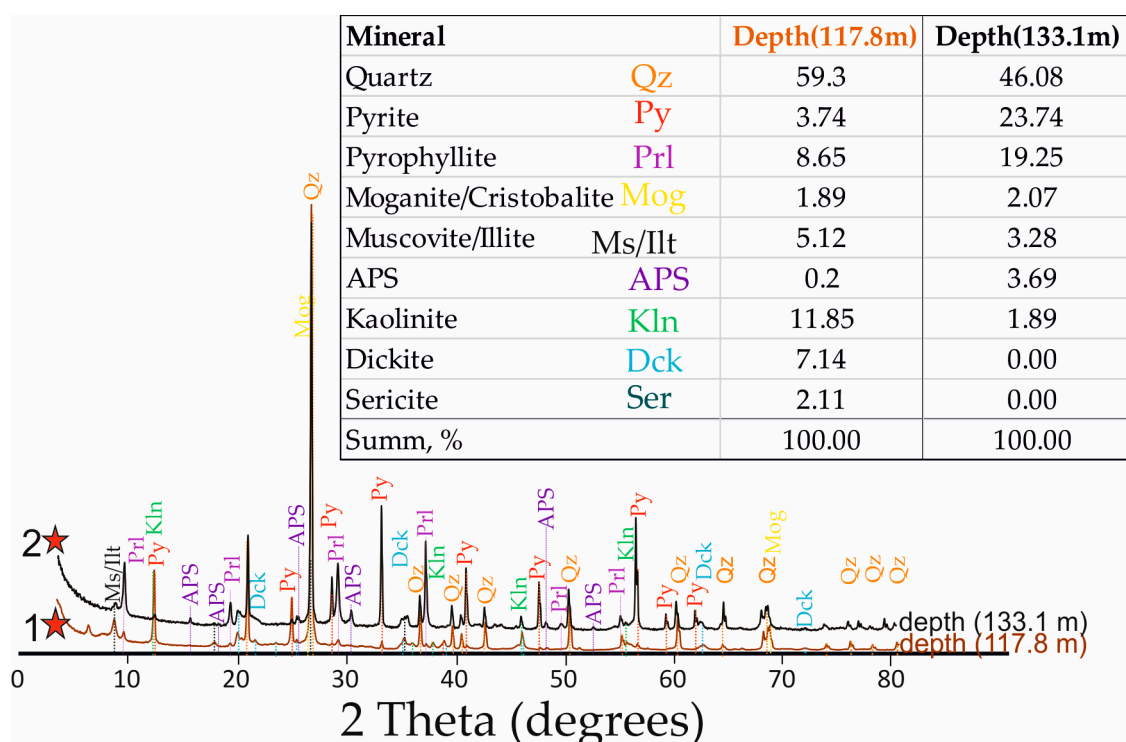


Figure 3. XRD patterns based on bulk composition of APS-bearing rocks. Sampling locations are shown by asterisks on the hydrothermal alteration map and the geological cross-section (AB) of Emmy deposit (see Figures 2a and 2b, respectively).

The APS minerals in the Emmy deposit are represented by the beudantitehinsdalite groups [30,34], and can be classified as calcian svanbergite, svanbergite, strontian woodhouseite, and plumbian woodhouseite (Table 2). They are characterized by a leached and uniform character, predominantly in the intermediate to outer parts (Figure 4). The central part of the APS grains, reflecting the process of apatite dissolution and replacement, is enriched in Sr and Ca (svanbergite and woodhouseite), rare earth elements (REE), and Ce, and is characterized by the irregular distribution of these components, causing a fluctuant vermiform randomly distributed pattern (Figure 5a,b). Following the leaching process and the goldfieldite–kawazulite–hemusite mineralization, which is associated with quartz (IIb), kaolinite/dickite, and pyrite IIb, a new hydrothermal pulse introduces gold and enriches the marginal parts of the APS grains with Pb and Ba, forming an oscillatory zoning pattern (Figures 4 and 5c,d). BSE data confirm a similar pattern of grains and demonstrate features of the internal structure of numerous APS grains (see Figure 4). This pattern of oscillatory zoning is also observed in barite, which is enriched in lead in some zones, where micron-sized grains of native gold are observed (Figure 6).

4.3. Petrography and Microthermometry of Fluid Inclusions

We studied samples of doubly polished sections containing quartz–pyrite–gol–feldite and gold–silver–telluride–polymetallic mineral association, which correspond to the ore hydrothermal stage. In the growth zones of euhedral crystalline quartz (generations IIb and III), primary (P) and secondary (S) fluid inclusions (FIs) were diagnosed (Figure 7a–f). Ore euhedral quartz (IIb and III) is saturated with gas–liquid inclusions to varying degrees. There are grains with many inclusions and pure grains, almost devoid of inclusions. Pseudosecondary (PS) inclusions are arranged linearly in the form of chains, confined to cutting cracks and crossing grain boundaries. They are also characterized by unlacing, reflected in the variable amount of liquid and gaseous phases.

Table 2. Representative electron probe microanalyses of APS minerals from the Emmy deposit (bd: below detection).

Nr	Al ₂ O ₃	P ₂ O ₅	SO ₃	CaO	SrO	BaO	La ₂ O ₃	Ce ₂ O ₃	Nd ₂ O ₃	PbO	Total	Formula:	Mineral
1	32.13	22.19	11.20	3.97	9.38	bd	1.94	3.46	0.85	bd	85.12	(Sr _{0.424} Ca _{0.332} Ce _{0.099} La _{0.056} Nd _{0.024}) Σ _{0.933} Al _{2.949} (PO ₄) _{1.463} (SO ₄) _{0.655} (OH _{4.096} ,H ₂ O _{1.90})	Ca-Svanbergite
2	34.02	23.65	10.72	2.23	13.45	bd	2.54	4.33	1.43	bd	92.36	(Sr _{0.672} Ca _{0.206} Ce _{0.137} La _{0.081} Nd _{0.044}) Σ _{1.14} Al _{2.956} (PO ₄) _{1.476} (SO ₄) _{0.593} (OH _{2.326} ,H ₂ O _{3.67})	Ca-Svanbergite
3	33.68	22.47	13.32	bd	21.16	bd	bd	bd	bd	bd	90.63	Sr _{1.02} Al _{2.941} (PO ₄) _{1.409} (SO ₄) _{0.741} (OH _{2.752} ,H ₂ O _{3.248})	Svanbergite
4	33.30	23.75	9.96	2.40	10.89	bd	2.31	4.55	2.36	bd	89.53	(Sr _{0.525} Ca _{0.214} Ce _{0.138} La _{0.063} Nd _{0.070}) Σ _{1.02} Al _{2.978} (PO ₄) _{1.526} (SO ₄) _{0.567} (OH _{3.075} ,H ₂ O _{2.93})	Ca-Svanbergite
5	29.69	21.58	9.16	1.25	12.98	bd	1.93	3.11	0.90	bd	80.60	(Sr _{0.572} Ca _{0.102} Ce _{0.087} La _{0.054} Nd _{0.024}) Σ _{0.839} Al _{2.95} (PO ₄) _{1.54} (SO ₄) _{0.579} (OH _{5.122} ,H ₂ O _{0.79})	Ca-Svanbergite
6	31.32	20.06	12.19	1.23	18.69	bd	bd	bd	bd	bd	83.49	(Sr _{0.839} Ca _{0.102}) Σ _{0.941} Al _{2.945} (PO ₄) _{1.355} (SO ₄) _{0.73} (OH _{4.52} ,H ₂ O _{1.48})	Ca-Svanbergite
7	32.49	22.65	11.10	2.07	13.40	bd	bd	2.29	bd	bd	84.00	(Sr _{0.595} Ca _{0.17} Ce _{0.064}) Σ _{0.828} Al _{2.999} (PO ₄) _{1.501} (SO ₄) _{0.652} (OH _{4.52} ,H ₂ O _{1.48})	Ca-Svanbergite
8	32.05	20.82	13.03	4.96	9.79	bd	1.35	2.69	0.72	bd	85.41	(Sr _{0.441} Ca _{0.413} Ce _{0.076} La _{0.039} Nd _{0.020}) Σ _{0.989} Al _{2.909} (PO ₄) _{1.357} (SO ₄) _{0.753} (OH _{4.00} ,H ₂ O _{1.99})	Ca-Svanbergite
9	31.69	22.06	10.38	2.48	11.73	bd	1.86	4.02	1.54	bd	86.64	(Sr _{0.552} Ca _{0.216} Ce _{0.119} La _{0.056} Nd _{0.045}) Σ _{0.988} Al _{2.949} (PO ₄) _{1.475} (SO ₄) _{0.615} (OH _{3.83} ,H ₂ O _{2.17})	Ca-Svanbergite
10	31.33	15.53	16.40	3.60	7.00	4.03	bd	bd	bd	11.46	89.54	(Sr _{0.355} Ca _{0.338} Pb _{0.27} Ba _{0.137}) Σ _{0.955} Al _{3.019} (PO ₄) _{1.075} (SO ₄) _{1.00} (OH _{3.238} ,H ₂ O _{2.76})	Ca-Svanbergite
11	32.36	22.28	9.76	2.00	12.28	bd	2.06	4.56	1.78	bd	87.08	(Sr _{0.581} Ca _{0.175} Ce _{0.136} La _{0.062} Nd _{0.052}) Σ _{1.00} Al _{2.985} (PO ₄) _{1.476} (SO ₄) _{0.573} (OH _{3.726} ,H ₂ O _{2.27})	Ca-Svanbergite
12	33.63	24.96	8.91	1.79	9.77	bd	3.43	6.32	2.35	bd	91.17	(Sr _{0.483} Ce _{0.197} Ca _{0.164} La _{0.108} Nd _{0.072}) Σ _{1.02} Al _{2.993} (PO ₄) _{1.596} (SO ₄) _{0.505} (OH _{2.662} ,H ₂ O _{3.338})	Ce-Svanbergite
13	34.47	22.99	11.88	5.54	5.02	0.49	2.41	3.87	1.25	bd	87.92	(Sr _{0.23} Ca _{0.469} Ce _{0.112} La _{0.070} Nd _{0.035} Ba _{0.015}) Σ _{0.915} Al _{3.02} (PO ₄) _{1.449} (SO ₄) _{0.664} (OH _{2.662} ,H ₂ O _{3.34})	Sr-Woodhouseite
14	35.70	25.23	10.87	6.44	4.98	bd	3.00	4.79	1.61	bd	92.62	(Ca _{0.575} Sr _{0.241} Ce _{0.146} La _{0.092} Nd _{0.048}) Σ _{1.102} Al _{2.977} (PO ₄) _{1.511} (SO ₄) _{0.577} (OH _{2.17} ,H ₂ O _{3.83})	Sr-Woodhouseite
15	29.67	12.49	16.69	4.96	bd	4.54	bd	bd	bd	13.40	81.74	(Ca _{0.420} Pb _{0.285} Ba _{0.141}) Σ _{0.706} Al _{3.051} (PO ₄) _{0.923} (SO ₄) _{1.093} (OH _{5.105} ,H ₂ O _{0.895})	Pb-Woodhouseite
16	34.67	15.41	19.31	5.73	1.30	5.24	bd	bd	bd	15.49	97.15	(Ca _{0.58} Pb _{0.394} Ba _{0.194} Sr _{0.071}) Σ _{1.045} Al _{3.008} (PO ₄) _{0.96} (SO ₄) _{1.067} (OH _{0.951} ,H ₂ O _{5.05})	Pb-Woodhouseite
17	31.67	14.00	18.26	5.16	1.36	5.75	bd	bd	bd	13.93	90.49	(Ca _{0.486} Pb _{0.329} Ba _{0.198} Sr _{0.069}) Σ _{0.884} Al _{2.978} (PO ₄) _{0.946} (SO ₄) _{1.093} (OH _{2.952} ,H ₂ O _{3.05})	Pb-Woodhouseite
18	31.53	12.13	20.91	5.43	bd	4.31	bd	bd	bd	10.75	86.75	(Ca _{0.475} Pb _{0.236} Ba _{0.138}) Σ _{0.711} Al _{3.033} (PO ₄) _{0.838} (SO ₄) _{1.281} (OH _{3.824} ,H ₂ O _{2.18})	Pb-Woodhouseite
19	31.35	13.57	18.18	5.44	bd	6.21	bd	bd	bd	11.78	86.54	(Ca _{0.468} Pb _{0.261} Ba _{0.20}) Σ _{0.741} Al _{3.016} (PO ₄) _{0.938} (SO ₄) _{1.114} (OH _{3.919} ,H ₂ O _{2.08})	Pb-Woodhouseite
20	30.17	12.70	17.70	4.38	bd	5.74	bd	bd	bd	15.68	86.38	(Ca _{0.397} Pb _{0.357} Ba _{0.19}) Σ _{0.754} Al _{3.015} (PO ₄) _{0.912} (SO ₄) _{1.126} (OH _{4.07} ,H ₂ O _{1.93})	Pb-Woodhouseite

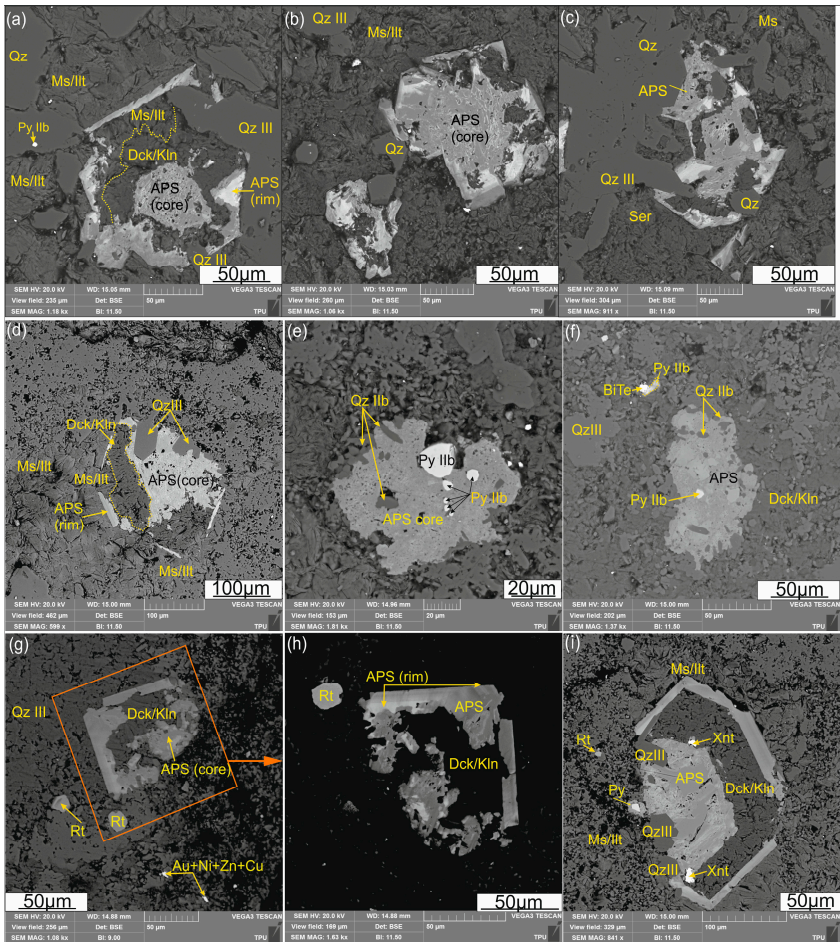


Figure 4. (a–i) Photomicrographs (SEM-BSE images) of aluminum phosphate–sulfate (APS) minerals from the Emmy deposit (samples collected at a depth of 117.8 m and marked by the first asterisk in Figure 1a, XRD bulk sample data (see Figure 5)). Associated minerals are pyrite (Py IIb), dickite/kaolinite (Dck/Kln), Ms/Ilt (muscovite/illite), xenotime (Xnt), rutile (Rtl), quartz (Qz IIb and III), tellurobismuthite (BiTe), and native gold with alloys of Ni,Zn,Cu (Au + Ni + Zn + Cu).

The shape of the vacuoles of such inclusions is irregular and amoeba-like. Primary (P) inclusions are rare and have the form of negative crystals of an elongated or rounded semi-faceted shape (Figure 7d). They are usually observed in the form of irregular accumulations in the central parts of quartz III grains.

In total, three types of fluid inclusions were identified, differing in phase composition at room temperature (Table 3).

Table 3. Results of microthermometric studies of two-phase and gas FIs in the Emmy deposit.

Incl. Type	N	T _h (°C)	T _m ise (°C)	Sal. (wt.% NaCl eq.)
Quartz–pyrite–goldfeldite mineral association				
Type I	42	337–310	−0.1–0.0	0.00–0.18
Gold–silver–telluride–polymetallic mineral association				
Type I	31	275–236	−0.1–−0.2	0.35–0.18

Note: N—number of measurements.

Type I—P and PS two-phase FIs have an oval or irregularly curved shape—size from a few microns to 10 microns. Thermometric studies reliably reveal the composition L_{H2O} + G_{H2O} (Figure 7a,b,e,f).

Type II—less common steam single-phase FIs (Figure 7c). As a rule, solitary.

Type III—less common PS FIs of $L_{H_2O} + G_{CO_2}$ (Figure 7d–g). Located along the crack. They are found in quartz IIb.

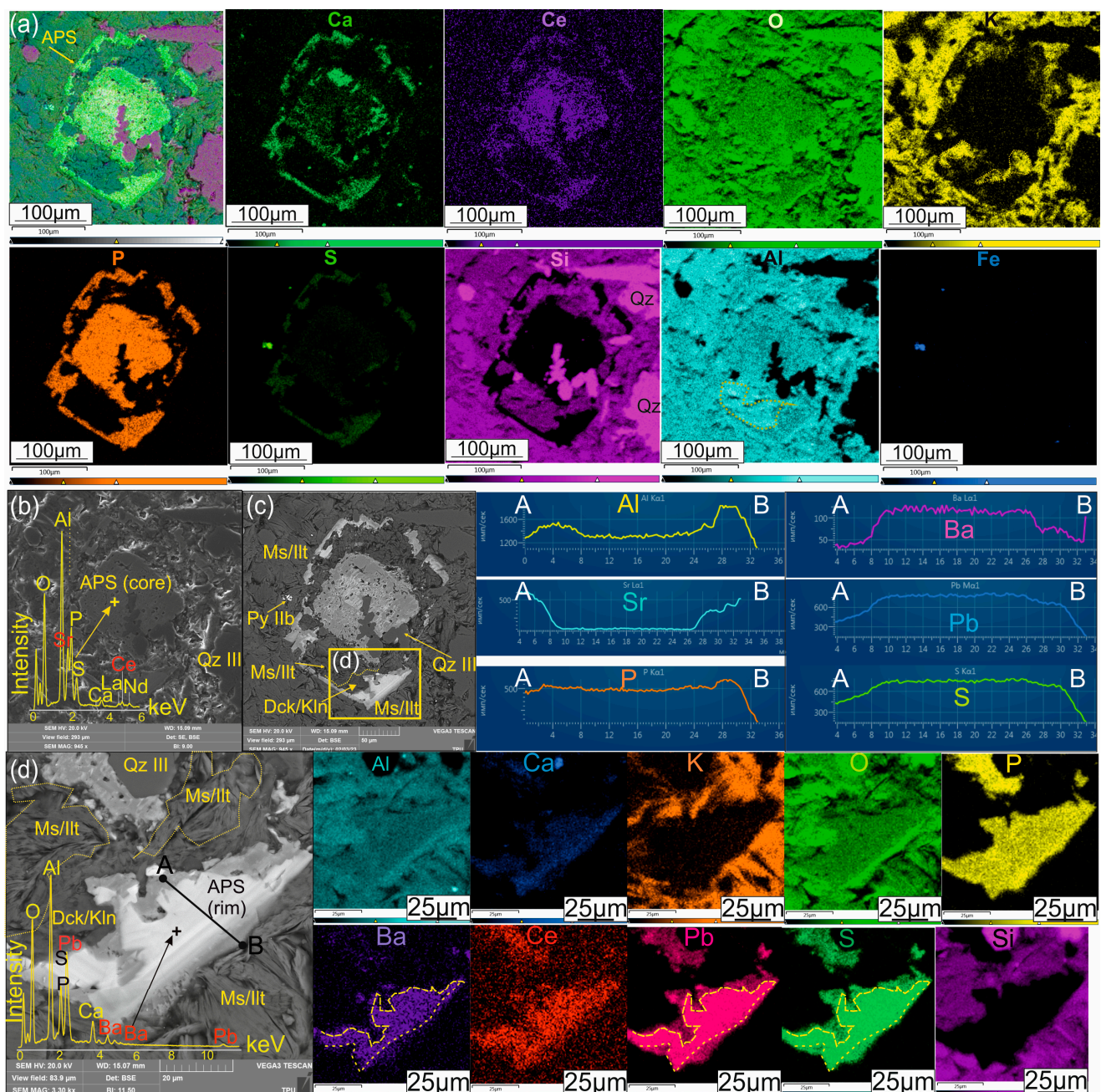


Figure 5. (a–d) Photomicrographs of aluminum phosphate–sulfate (APS) minerals in secondary (b) and backscattered (c–d) electrons. Multi-element maps illustrate the distribution of Ca, Ce, K, P, S, Al, Si, Fe, Ba, Pb, and O within the APS grain and its enlarged fragment. The profile AB reflects the concentration of trace elements in the absorption edge. Ms/Ilt—muscovite/illite, Dck/Kln—dickite/kaolinite, Py—pyrite, and Qz III—quartz.

Microthermometric studies were carried out on type I inclusions. The results are presented in Table 3. Homogenization temperatures for quartz–pyrite–goldfieldite mineral association vary within 337–310 °C and salinity within 0–0.18 wt.% NaCl equivalent. These data were determined for quartz IIb with pyrite IIb inclusions (Figure 7a). According to Raman spectroscopy data, the gas phase in quartz IIb FIs is represented by carbon dioxide

(Figure 7g). Homogenization temperatures for gold–silver–telluride–polymetallic mineral association decrease and vary within 275–236 °C and salinity slightly increases from 0.18 to 0.35 wt.%NaCl equivalent.

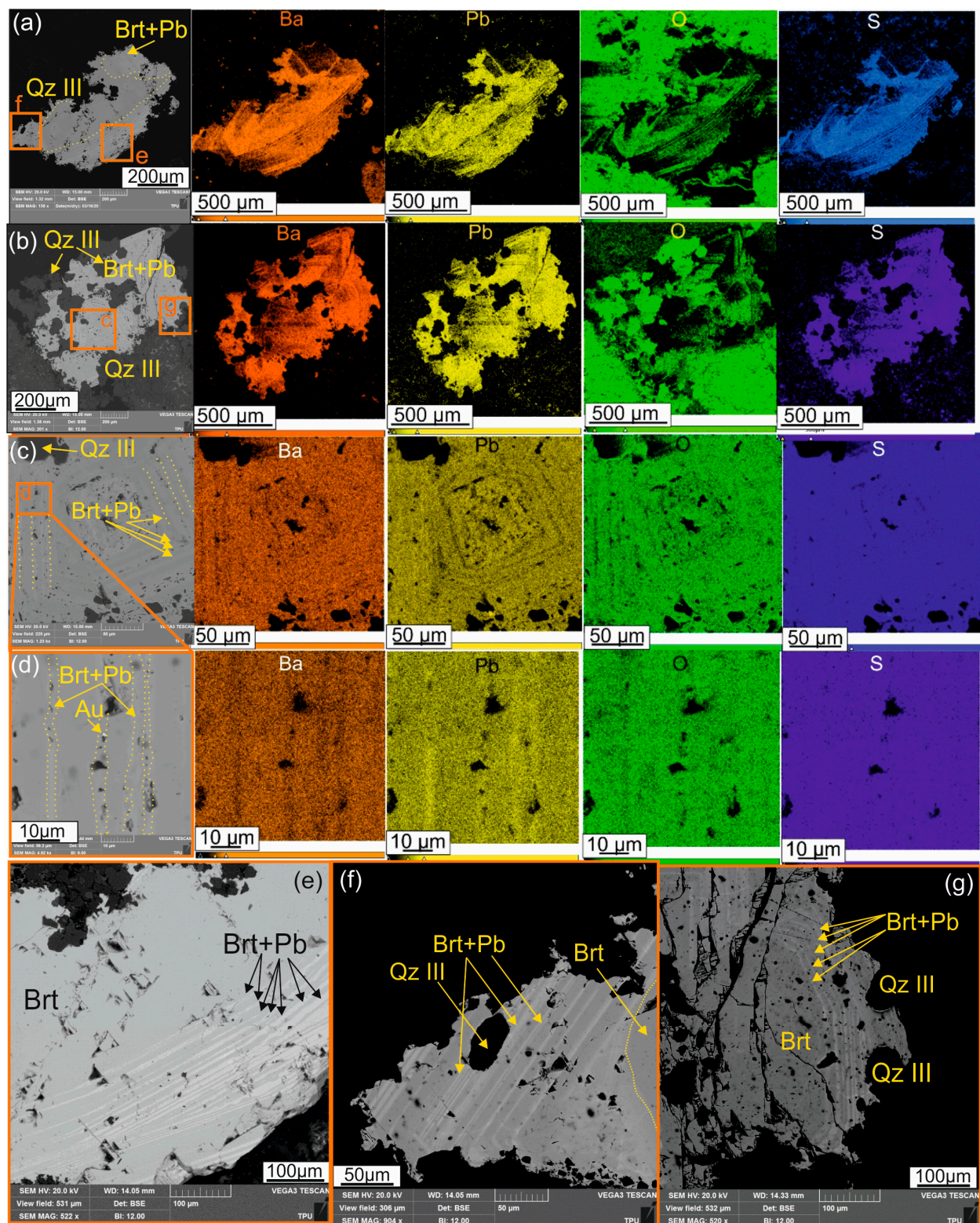


Figure 6. (a–g) Photomicrographs of barite (Brt) in backscattered electrons. Multi-element maps illustrate the distribution of Ba, Pb, O, and S within its grains, and its enlarged fragments demonstrate oscillatory zonation resulting from the enrichment of individual barite zones with lead (Brt + Pb). Qz III—quartz, Au—native gold.

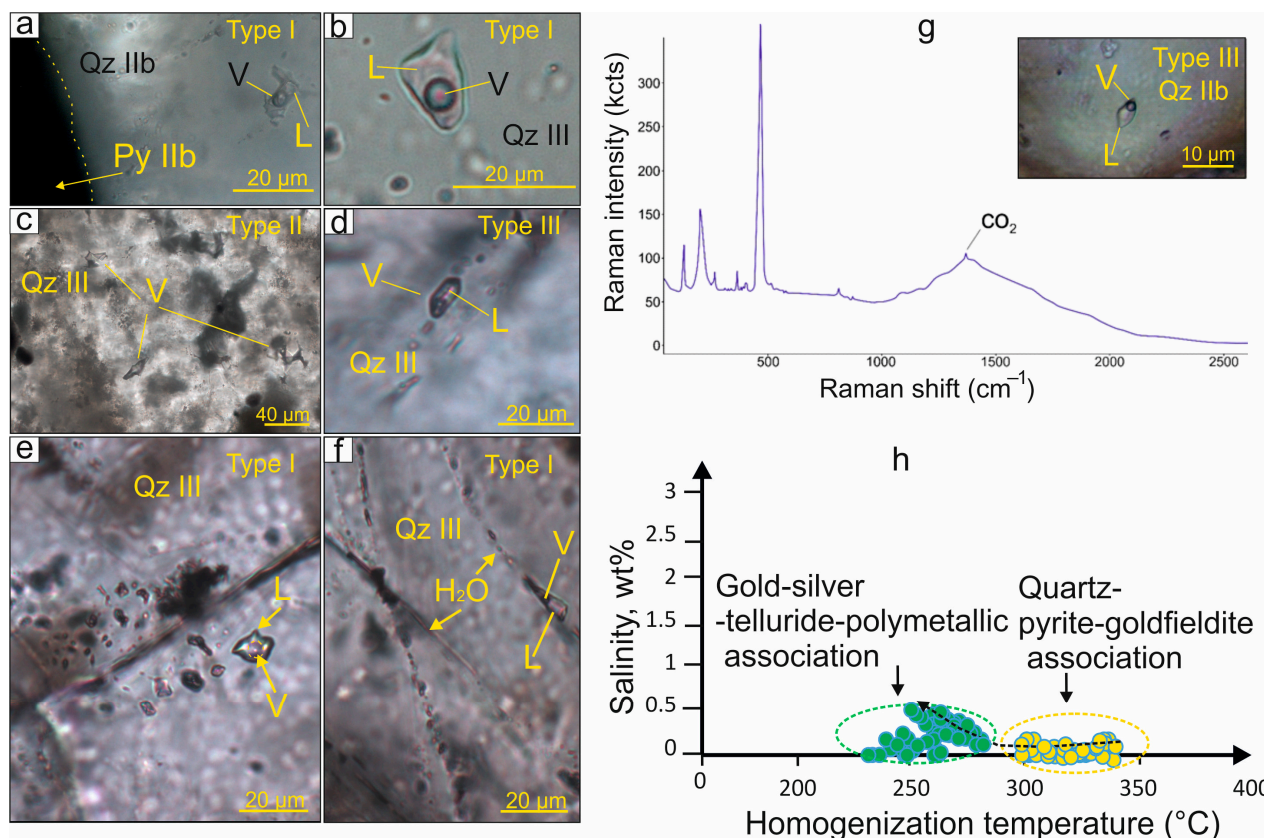


Figure 7. (a–f) Microphotographs of secondary vapor–liquid (a,e–f), represented by water (H₂O), observed within the quartz (Qz IIb, III) in the Emmy deposit, and primary vapor(V)–liquid(L) (b–d) and vapor (c) fluid inclusions hosted in quartz (Qz III), (g) Raman spectra of carbon dioxide reflecting gas composition of the pseudosecondary two-phase liquid- and vapor-rich inclusion in quartz IIb; summary histogram of homogenization temperatures–salinity pair (h) for inclusions of the Emmy deposit.

5. Discussion

5.1. Sulfosalts

Tetrahedrite group minerals (TGMs) [27] are a widespread group of sulfosalts in hydrothermal gold deposits that can be sensitive indicators of the composition of the initial solutions involved in the formation of deposits. They are formed from hydrothermal solutions at temperatures of more than 100 and less than 400 °C (usually 200–300 °C) and a pressure of no more than 4 kbar [39–44]. Given the ability of TGMs to form solid solutions, they are a suitable petrogenetic tool for determining the environment of mineral formation [43,45–47]. The composition of TGMs can directly depend on the composition of the metal-bearing solutions involved in the formation of deposits. Therefore, the composition of the TGMs and the nature of their internal structure can be used as an indicator of the physicochemical conditions at the time of mineral formation [48]. Goldfieldite is one of the very rare minerals. Goldfieldite [41] attracts attention in this paper due to its important role in the mineralization; it provides physicochemical constraints on ore formation, which help us to understand trace element distribution and fluid flow paths within the deposit, and can be used to aid mineral exploration [42,43]. Recently, two varieties of goldfieldite have been approved by the IMA, namely, stibio-goldfieldite [44] and arseno-goldfieldite [45]. Goldfieldite formation should occur at a relatively high oxygen potential and in a relatively acidic (pH up to 3–5) environment. Such conditions are common in the formation of mineralization at shallow depths. The oscillatory zoning of goldfieldite in the Emmy deposit

is represented by multiphase zonality, provided that the number and location of zones in the central part of different crystals from the same polished section is repeated. This fact indicates that the reason for such zoning lies not only in internal but in external factors, leading to the transition of Te from oxidized states in goldfieldite into neutral (Te^0 native tellurium) and then reduced (Te^{2-} in tellurides) [26].

The formation of oscillatory zoning of sulfosalts (tetrahedrite group minerals) in the epithermal Emmy deposit is attributed to chemical disequilibrium conditions, which may appear in an open system. A similar composition of goldfieldite is also characteristic of the Pefka and St. Demetrios/Sapes high- and intermediate-sulfidation deposits in northeastern Greece [45].

Hence, according to the modeling provided by T. Holten [25], oscillatory mineral zonation is usually associated with crystal growth in an open system and is characterized by non-equilibrium states or a hydrothermal system after a period of either mixing or degassing. They examined the effects of noisy boundary conditions on four different crystal growth models and decided that the observed pattern may be a direct consequence of spatial and temporal fluctuations in the environment where minerals formed. Oscillatory intracrystalline mineral zonation almost invariably occurs in an open system, with a continuous or discontinuous mass flux into or through the crystal growth region [25]. Consequently, it is expected that many natural patterns, including mineral zonation patterns, are affected by noise and system heterogeneities. Noise need not be restricted to fluctuations in the concentration of the crystal-forming components, but can also be associated with fluctuations in other intensive variables such as oxygen fugacity, pH, and temperature. However, pattern formation would not occur without the internal autonomous nonlinear dynamics of the system [25]. For example, goldfieldite from various deposits exhibits oscillatory zoning, while other TGMs are rarely characterized by it [49]. Oscillations can be associated with periodic pressure releases or mixing in geothermal fields [24,25,50]. According to [45,51], inclusions of native Te and tellurides were not contemporaneous to goldfieldite. However, they were instead the result of the new influx of volatiles and metals/metalloids in the system during hydrothermal post-volcanic activity. This study suggests that by the time the new fluid impulse was introduced in the Emmy deposit, the stibio-goldfieldite crystals had not yet completely crystallized, as evidenced by plastic deformations and continued grain growth. The new influx was also enriched in addition to metals (Au, Ag, Hg, and other elements).

5.2. Sulfates

APS minerals are represented in the Emmy deposit by svanbergite $\text{SrAl}_3(\text{P}_{0.5}\text{S}_{0.5}\text{O}_4)_2(\text{OH})_6$, woodhouseite $\text{CaAl}_3(\text{P}_{0.5}\text{S}_{0.5}\text{O}_4)_2(\text{OH})_6$ in the central part of APS grains, and plumbian woodhouseite $\text{CaAl}_3(\text{P}_{0.5}\text{S}_{0.5}\text{O}_4)_2(\text{OH})_6$ in the rims, according to the classification of Scott [28], Dill [52], and Mills et al. [32]. The APS minerals can also be formed during weathering [53]; these minerals in the Emmy deposit have a hypogene genesis, as they are intimately associated with crystalline pyrite IIb (see Figure 4). Their formation is related to the transformation of magmatic apatite, firstly into monazite or xenotime and then to APS, in the deep levels of the advanced argillic alteration zone, in accordance with observations elsewhere (i.e., [54,55]) (see Figures 4 and 5).

The APS minerals occur within zones of advanced argillic and transitional advanced argillic to sericitic alteration zones in several porphyry and high-sulfidation epithermal deposits in, for example, Lepanto [3], Baquío [56], El Salvador [57], Summitville, La Granja, La Escondida [58], and Melitena and Sapes [19,59]. Analysis of APS mineral compositions can reveal useful information regarding local conditions of formation with respect to fluid composition, pH, and $f\text{O}_2$ [58].

The central parts of aluminum phosphate–sulfate (APS) minerals present in the Emmy deposit are Ca-Sr-Ce-dominant APS minerals that fall within the *svanbergite*–*woodhouseite* compositional field. These parts of APS minerals in the Emmy deposit were deposited during an initial stage of primary apatite and alkali earth elements dissolution by acid solutions of magmatic–hydrothermal origin, as suggested by Stoffregen and Alpers [58]. Subsequent hydrothermal alteration in the Emmy deposit leaches these grains, due to the interaction of reactive acidic solutions in the system, resulting in the crystallization of plumbian *woodhouseite* in the rims of the APS grains.

In the analysis of elemental maps and due to the results of the distribution of elements within the studied grains of APS, it was found that sulfur, together with lead and barium, enriches the marginal zone, characterized by oscillatory zoning. In contrast, the central part of the grains is enriched with cerium, strontium, and calcium. Between these two parts of the crystals, there is a break or a sharp change in crystallization conditions, possibly due to the process of mixing of the fluid, accompanied by precipitation of the mineralization, which is associated with *pyrite* IIb, *goldfieldite*, *kawazulite*, and *hemusite*. This crystallization of Pb-bearing APS minerals (i.e., *hinsdalite*) with *pyrite* occurs in the Summitville gold–copper deposit (Colorado) [58] and the Mavrokoryfi HS silver–gold–copper deposit (Greece) [59]. The marginal parts of APS minerals in the Emmy deposit exhibit preferential sorption of Pb. This enrichment may indicate proximity to a porphyry-style mineralization at depth, as stated for the Melitena porphyry–epithermal deposit (Greece) by Voudouris and Melfos [60]. Similarly, the *svanbergite*–*woodhouseite* solid solution series of APS minerals with a similar internal structure and zoning is associated with the moderately to highly mineralized quartz veins of the Kuh-e-Lakht lithocap NE Isfahan, Iran [61].

Since we observe a repeating pattern of oscillating texture in different grains of APS minerals in the studied material, we conclude that these textures are the result of external conditions, i.e., the behavior of the general ore-forming hydrothermal process, and that they are not related with the internal self-organization of individual APS grains. In the latter case, the grains should have a more individual internal structure without a regular alternation of zones.

In the upper parts of the advanced argillic alteration zone, *barite*, similarly to APS minerals demonstrates oscillatory zonation within the grains and exhibit preferential sorption of Pb, confirming a change in external conditions of mineralization process of the Emmy deposit.

5.3. Microthermometry of Fluid Inclusions

According to the study of FIs in quartz IIb and III within the Emmy deposit, a slightly saline fluid flow is noted at the modern level of the erosion section. Despite the almost flat trend in the salinity–temperature graph (see Figure 7), a slightly raised upward trend can indirectly indicate possible mixing processes. The textural and structural features of ore and vein minerals indicate their sharp and rapid precipitation, and then slow crystallization. However, this fact is definitely not confirmed by our limited FI data. The solubility of silica drops sharply, and amorphous and cryptocrystalline quartz (*moganite*, according to the XRD bulk data) with collomorphic and croustification-striped textures is deposited, which may indirectly indicate mixing processes. However, such a variety of quartz is not favorable for capturing primary fluid inclusions. Therefore, only crystalline quartz (IIb and III) were studied. Within the limits of the Emmy deposit, the hydrothermal ore process forming the productive mineral associations took place at a temperature of 236–337 °C.

The quartz–*pyrite*–*goldfieldite*–*hemusite* mineral association was formed in the temperature range of 337–310 °C, while the gold–silver–telluride–polymetallic one was formed within 275–236 °C.

According to Li Wang [62], deposits of a moderately acidic type often have a close relationship with andesite–dacite volcanogenic–subvolcanic rocks formed in subduction environments at depths from 300 to 1000 m, as a result of calcareous-alkaline magmatism. The homogenization temperatures of gas–liquid inclusions vary from 150 to 350 °C [62,63], similar to the data we obtained during microcryothermometric experiments. According to [64], most Au–Ag epithermal deposits are characterized by low salinity (<5 wt.%), with dilute fluid and homogenization temperatures of FIs ~ 200–300 °C.

5.4. Paragenetic Sequence

Based on mineralogical and petrographic studies of sulfosalts (goldfieldite) and sulfates (APS minerals and barite) we suggest that within the Au–Ag–Te Emmy deposit, the periods of rapid deposition of ore are due to the mixing of solutions with meteoric water, followed by long-lasting conditions of mineral formation in an open ore-forming system.

The most common sulfide, especially in gold deposits, is traditionally considered to be pyrite [65–68]. The Emmy deposit is no exception, in which the main sulfide is pyrite, which occurs in several generations and crystal forms:

- (i) Pre-ore pyrite (I) with cubic habit is fine-grained, with an average crystal size from 20–50 µm to 500 µm. It is almost pure pyrite and corresponds to the early barren stage (Supplementary Figure S2a). Pyrite (I) hosts inclusions of galena, sphalerite, tetrahedrite group minerals (TGMs), carbonates, and quartz, filling voids in the process of further mineral formation;
- (ii) Pyrite (II) from the ore stage is represented by two morphological varieties—colloform (IIa) (Supplementary Figure S2b), most likely earlier, which is overgrown by crystalline (idiomorphic) pyrite (IIb) (Supplementary Figure S2c). Both morphological varieties contain Cu (0.06–6.03 wt %). Pyrite of this stage occurs in association with goldfieldite (Supplementary Figure S2b), hemusite (Supplementary Figure S2c,d), and kawazulite (Supplementary Figure S2e), and is replaced by tetrahedrite–tennantite, chalcopyrite (Supplementary Figure S2f–i), gold, silver, and other tellurides (Supplementary Figure S2g–m), suggesting an influx of later fluids enriched in Cu, Ni, Pb, Hg, Au, Ag, and tellurium. Crystalline pyrite (IIb) has euhedral crystal habit that deviates from cubic depending on the depth of formation. For example, at deeper levels, pyrite (IIb) is represented by pentagondodecahedrons (i.e., pyritohedron) (Supplementary Figure S2j), whereas, towards the surface, it acquires a predominantly prismatic shape. Pyrite IIb also displays chemical heterogeneity with respect to its depth of formation; it is practically pure at the deepest levels and contains copper at intermediate depths (~38–46 m), where it is associated with colloform pyrite (IIa), and it is enriched with arsenic close to the surface [22].

According to the RDA data, copper-bearing pyrite of a collomorphic texture [22] (Supplementary Figures S1 and S2) associated with cryptocrystalline moganite may indicate a rapid precipitation process during abrupt cooling due to mixing with meteoric water. The subsequent formation of euhedral crystals of Cu-bearing pyrite bordering the colloform pyrite is attributed to a slow crystallization in a quiescent formation environment. Under these conditions, the system was possibly open, as evidenced by the oscillatory-zoned goldfieldite, accompanying crystalline Cu-bearing pyrite, emphasizing the rhythmic change in growth zones of enrichment in either arsenic or tellurium. A similar textural pattern, confirming the presence of a non-equilibrium state of the Emmy deposit, was found by studying euhedral quartz (IIb and III) and APS minerals in the marginal parts of the grains using cathodoluminescence.

The following schematic paragenetic sequence was developed (Figure 8) to visualize the identification of several stages of mineral formation within the Au–Ag–Te Emmy deposit.

According to this sequence, an early pre-ore alteration stage is followed by Cu-bearing mineralization, including an early Sn-Mo-Bi-Se-Te-rich (goldfieldite, hemusite, and kawazulite) stage, followed by a later As-Sb-Pb-Zn-Au-Ag-Ni-Hg-Bi-Te-rich (tetrahedrite–tennantite, galena, chalcopyrite, tellurides, and native Au) stage. All these stages are within the stability fields of APS minerals. Goldfieldite can form as part of IS ore assemblages in porphyry-epithermal deposits. However, it is also a characteristic mineral in HS mineralogical assemblages [41,46]. With typical HS minerals such as enargite, luzonite, and famatinite, we can classify the goldfieldite–hemusite–kawazulite assemblage as HS type. However, we suggest here an HS affinity for this assemblage, due to its intimate relationship with kaolinite/dickite and pyrophyllite in the Emmy deposit. The paragenetic sequence demonstrates an evolution of the system towards lower sulfidation states and more reducing conditions with time.

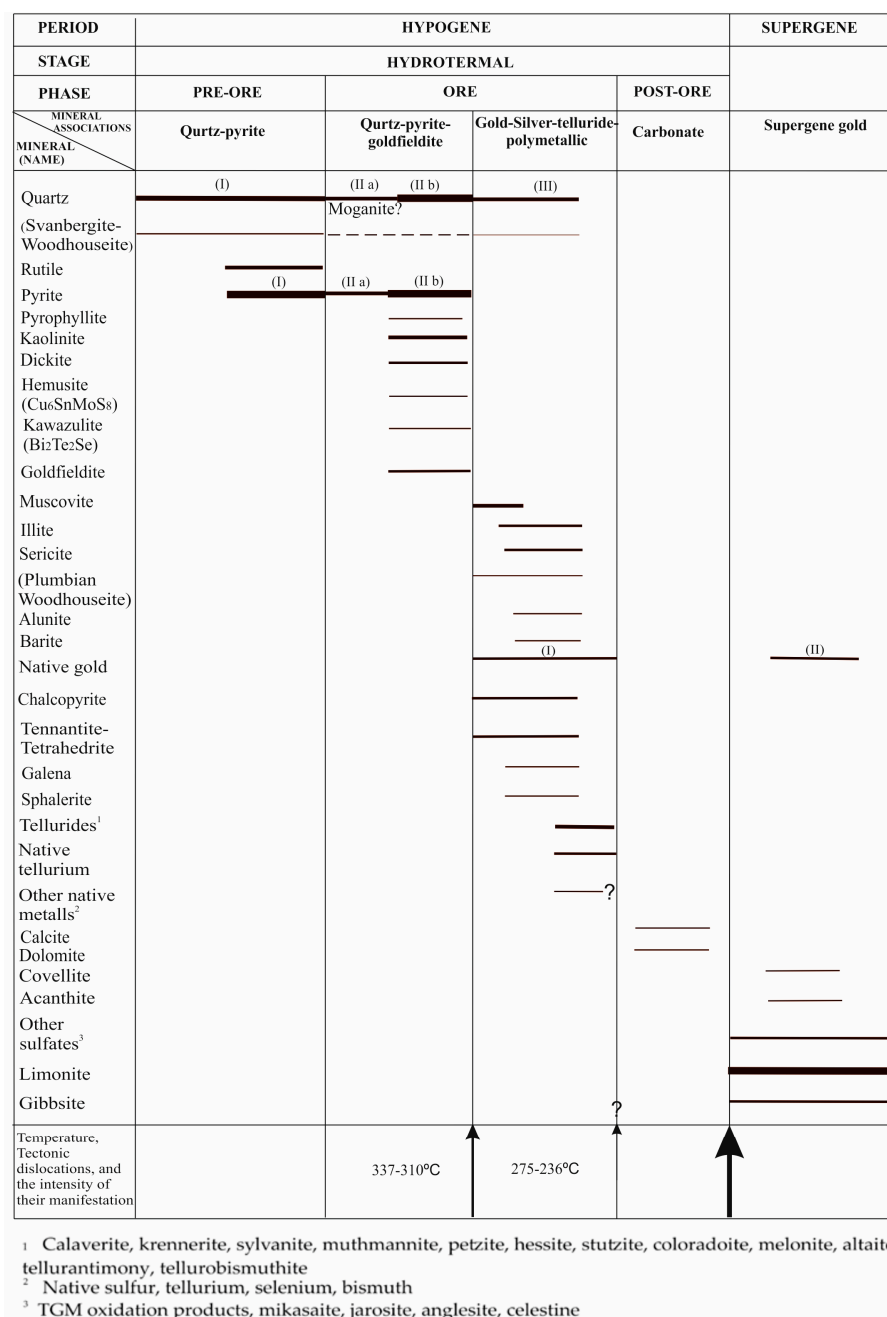


Figure 8. Paragenetic sequence of the Au-Ag-Te Emmy deposit demonstrating mineralogical evolution with time.

6. Conclusions

- (1) Based on mineralogical and petrographic studies of sulfosalts (goldfieldite) and sulfates (APS minerals and barite), we suggest possible scenarios within the most productive horizons of ore deposition within the Au-Ag-Te Emmy deposit, and that periods of rapid ore deposition due to the mixing of solutions with meteoric water were followed by long-lasting mineral formation conditions in an open ore-forming system.
- (2) Oscillatory-zoned goldfieldite is part of a HS mineral association in the Emmy deposit, followed by an IS assemblage composed of the tennantite–tetrahedrite group, tellurides, and native tellurium corresponding to a new influx of Te, Sb, and As.
- (3) Members of the svanbergite–woodhouseite series represent the APS minerals, and can be classified as calcian svanbergite, svanbergite, strontian woodhouseite, and plumbian woodhouseite. The core of the APS grains is enriched in cerium and strontium and was formed during the pre-ore stage due to apatite replacement. The intermediate part of the APS grains is leached vs. the deposition of goldfieldite–kawazulite–hemusite assemblage, respectively. The APS minerals' rim indicated lead enrichment in the marginal, oscillatory-zoned part of the grains, related to the gold–silver–telluride–polymetallic association of the mineralization, i.e., the late influx of IS fluids.
- (4) Barite found in the upper level of the advanced argillic alteration zone is characterized by oscillatory zoning and the lead enrichment of individual zones.
- (5) The study of fluid inclusions in quartz within the Emmy deposit showed that the hydrothermal ore process takes place at a temperature of 236–337 °C. Homogenization temperatures for quartz–pyrite–goldfieldite mineral association vary within 337–310 °C, and salinity varies within 0–0.18 wt.%NaCl equivalent, and for gold–silver–telluride–polymetallic mineral association, they decrease and vary within 275–236 °C, and salinity slightly increases from 0.18 to 0.35 wt.%NaCl equivalent.
- (6) This study demonstrates the fundamental importance of external processes, as reflected by the evolution of the physicochemical conditions of mineral formation.

Supplementary Materials: The following supporting information can be downloaded at: <https://www.mdpi.com/article/10.3390/geosciences15010026/s1>.

Author Contributions: Conceptualization, supervision, project administration, investigation, and writing—original draft preparation, T.Y.Y.; writing—review, recalculation of APS mineral formulas, formulation of some important ideas, and editing, P.V.; methodology, resources, development of a map of alteration zoning, and data curation, D.V.L.; carrying out bulk XRD analysis, M.V.S.; and its interpreting result, Y.M.L.; funding acquisition, reception, and synthesis of study data, M.A.R. and A.S.R.; data curation and analysis of text, A.K.M.; data curation and English editing, E.D.; sample preparation, P.N.M.; analytical data, K.V.B.; interpretation of FI data, E.A.S. All authors have read and agreed to the published version of the manuscript.

Funding: The research was supported by the Ministry of Science and Higher Education of the Russian Federation (project FSWW-2023-0010).

Data Availability Statement: The original contributions presented in this study are included in the article/Supplementary Material. Further inquiries can be directed to the corresponding author.

Acknowledgments: The authors thank the editor and four anonymous reviewers for their constructive reviews, which led to the improvement of the manuscript. The authors also thank Olga Y. Plotinskaya for advice on recalculating the composition of TGM.

Conflicts of Interest: Author Yuriy M. Lopushnyak was employed by the company LLC “NPP Qualitet”. The remaining authors declare that the research was conducted in the absence of any commercial or financial relationships that could be construed as a potential conflict of interest.

References

1. Sillitoe, R.H.; Thompson, J.F.H. Intrusion-Related Vein Gold Deposits: Types, Tectono-Magmatic Settings and Difficulties of Distinction from Orogenic Gold Deposits. *Resour. Geol.* **1998**, *48*, 237–250. [\[CrossRef\]](#)
2. Hedenquist, J.W.; Izawa, E.; Arribas, A., Jr.; White, N.C. Epithermal Gold Deposits: Styles, Characteristics, and Exploration: Resource Geology Special Publication. *SEG Newsl. Is.* **1995**, *23*, 9–13.
3. Hedenquist, J.W.; Arribas, A.; Reynolds, T.J. Evolution of an Intrusion-Centered Hydrothermal System: Far Southeast-Lepanto Porphyry and Epithermal Cu-Au Deposits, Philippines. *Econ. Geol.* **1998**, *93*, 373–404. [\[CrossRef\]](#)
4. Yakich, T.Y.; Nikolaeva, A.N.; Bukhanova, D.S.; Maximov, P.N.; Sinkina, E.A.; Kuttyrev, A.V.; Sarsekeeva, E.M.; Zhegunov, P.S.; Levochskaya, D.V.; Rudmin, M.A. Mineral Features of the Copper Association of the Baranovskoe Epithermal Deposit (Central Kamchatka). *Bull. Tomsk Polytech. Univ. Geo Assets Eng.* **2022**, *333*, 74–87. [\[CrossRef\]](#)
5. Levochskaya, D.V.; Yakich, T.Y.; Lesniak, D.V.; Ananyev, Y.S. Hydrothermal-Altered Zoning, Fluid Conditions, and Types of Gold Mineralization within the Elena and Emy Deposits of the Epithermal Svetloye Ore District (Khabarovsk Territory). *Bull. Tomsk Polytech. Univ. Geo Assets Eng.* **2021**, *332*, 17–32. [\[CrossRef\]](#)
6. König, S.; Eickmann, B.; Zack, T.; Yierpan, A.; Wille, M.; Taubald, H.; Schoenberg, R. Redox Induced Sulfur-Selenium Isotope Decoupling Recorded in Pyrite. *Geochim. Cosmochim. Acta* **2019**, *244*, 24–39. [\[CrossRef\]](#)
7. Hattori, K.H.; Arai, S.; Clarke Barrie, D.B. Selenium, Tellurium, Arsenic and Antimony Contents of Primary Mantle Sulfides. *Can. Mineral.* **2002**, *40*, 637–650. [\[CrossRef\]](#)
8. Helmy, H.M.; Ballhaus, C.; Berndt, J.; Bockrath, C.; Wohlgemuth-Ueberwasser, C. Formation of Pt, Pd and Ni Tellurides: Experiments in Sulfide-Telluride Systems. *Contrib. Mineral. Petrol.* **2007**, *153*, 577–591. [\[CrossRef\]](#)
9. Marfin, A.E.; Ivanov, A.V.; Abramova, V.D.; Anziferova, T.N.; Radomskaya, T.A.; Yakich, T.Y.; Bestemianova, K.V. A Trace Element Classification Tree for Chalcopyrite from Oktyabrsk Deposit, Norilsk–Talnakh Ore District, Russia: La-Icpms Study. *Minerals* **2020**, *10*, 716. [\[CrossRef\]](#)
10. Börner, F.; Keith, M.; Bucker, J.; Voudouris, P.; Klemd, R.; Haase, K.; Kutzschbach, M. In-Situ Trace Element and S Isotope Systematics in Porphyry-Epithermal Pyrite, Limnos Island, Greece. *Front. Earth Sci.* **2021**, *10*. [\[CrossRef\]](#)
11. Cook, N.J.; Ciobanu, C.L.; Spry, P.G.; Voudouris, P. Understanding Gold-(Silver)-Telluride-(Selenide) Mineral Deposits. *Episodes* **2009**, *32*, 249–263. [\[CrossRef\]](#)
12. Spry, P.G.; Foster, F.; Truckle, J.S.; Chadwick, T.H. The Mineralogy of the Golden Sunlight Gold-Silver Telluride Deposit, Whitehall, Montana, U.S.A. *Mineral. Petrol.* **1997**, *59*, 143–164. [\[CrossRef\]](#)
13. Pals, D.W.; Spry, P.G.; Chrysoulis, S. Invisible Gold and Tellurium in Arsenic-Rich Pyrite from the Emperor Gold Deposit, Fiji: Implications for Gold Distribution and Deposition. *Econ. Geol.* **2003**, *98*, 479–493. [\[CrossRef\]](#)
14. Cook, N.J.; Ciobanu, C.L.; Mao, J. Textural Control on Gold Distribution in As-Free Pyrite from the Dongping, Huangtuliang and Hougou Gold Deposits, North China Craton (Hebei Province, China). *Chem. Geol.* **2009**, *264*, 101–121. [\[CrossRef\]](#)
15. Cooke, D.R.; McPhail, A.D.C. Epithermal Au-Ag-Te Mineralization, Acupan, Baguio District, Philippines: Numerical Simulations of Mineral Deposition. *Econ. Geol.* **2001**, *96*, 109–131.
16. Cook, N.J.; Ciobanu, C.L. Bismuth Tellurides and Sulphosalts from the Larga Hydrothermal System, Metaliferi Mts, Romania: Paragenesis and Genetic Significance. *Mineral. Mag.* **2004**, *68*, 301–321. [\[CrossRef\]](#)
17. Kovalenker, V.A.; Safonov, Y.G.; Naumov, V.B.; Rusinov, V.L. The Epithermal Gold-Telluride Kochbulak Deposit (Uzbekistan). *Geol. Ore Depos.* **1997**, *39*, 107–128.
18. Plotinskaya, O.Y.; Kovalenker, V.A.; Seltmann, R.; Stanley, C.J. Te and Se Mineralogy of the High-Sulfidation Kochbulak and Kairagach Epithermal Gold Telluride Deposits (Kurama Ridge, Middle Tien Shan, Uzbekistan). *Mineral. Petrol.* **2006**, *87*, 187–207. [\[CrossRef\]](#)
19. Voudouris, P.; Melfos, V. Aluminum-Phosphate-Sulfate (APS) Minerals in the Sericitic-Advanced Argillic Alteration Zone of the Melitena Porphyry-Epithermal Mo-Cu ± Au ± Re Prospect, Western Thrace, Greece. *Neues Jahrb. Mineral.* **2013**, *190*, 11–27. [\[CrossRef\]](#) [\[PubMed\]](#)
20. Sidorov, E.G.; Borovikov, A.A.; Tolstykh, N.D.; Bukhanova, D.S.; Palyanova, G.A.; Chubarov, V.M. Au (Ag)-Se-Te-S-Cu-Sb-As-Bi Mineralization at the Maletoyvayam Deposit (Central Kamchatka, Russia) and Physicochemical Conditions of Its Formation. *Minerals* **2020**, *10*, 1093. [\[CrossRef\]](#)
21. Tolstykh, N.D.; Palyanova, G.A.; Bobrova, O.V.; Sidorov, E.G. Mustard Gold of the Gaching Ore Deposit (Maletoyvayam Ore Field, Kamchatka, Russia). *Minerals* **2019**, *9*, 489. [\[CrossRef\]](#)
22. Yakich, T.Y.; Ananyev, Y.S.; Ruban, A.S.; Gavrillov, R.Y.; Lesnyak, D.V.; Levochskaia, D.V.; Savinova, O.V.; Rudmin, M. Mineralogy of the Svetloye Epithermal District, Okhotsk-Chukotka Volcanic Belt, and Its Insights for Exploration. *Ore Geol. Rev.* **2021**, *136*, 104257. [\[CrossRef\]](#)
23. Ortoleva, P.; Merino, E.; Moore, C.; Chadam, J. Geochemical Self-Organization I; Reaction-Transport Feedbacks and Modeling Approach. *Am. J. Sci.* **1987**, *287*, 979–1007. [\[CrossRef\]](#)
24. Shore, M.; Fowler, A.D. Oscillatory Zoning in Minerals: A Common Phenomenon. *Can. Mineral.* **1996**, *34*, 1111–1126.

25. Holten, T.; Jamtveit, B.; Meakin, P. Noise and Oscillatory Zoning of Minerals. *Geochim. Cosmochim. Acta* **2000**, *64*, 1893–1904. [\[CrossRef\]](#)
26. Plotinskaya, O.Y.; Rusinov, V.L.; Kovalenker, V.A.; Seltnmann, R. Oscillatory Zoning in Goldfieldite as a Possible Indicator of It's Formation Conditions. *Bulg. Acad. Sci. Geochem. Mineral. Petrol.* **2005**, *43*, 142–147.
27. Biagioni, C.; George, L.L.; Cook, N.J.; Makovicky, E.; Moëlo, Y.; Pasero, M.; Sejkora, J.; Stanley, C.J.; Welch, M.D.; Bosi, F. The Tetrahedrite Group: Nomenclature and Classification. *Am. Mineral.* **2020**, *105*, 109–122. [\[CrossRef\]](#)
28. Scott, K.M. Solid Solution in, and Classification of, Gossan-Derived Members of the Alunite-Jarosite Family, Northwest Queensland, Australia. *Am. Mineral.* **1987**, *72*, 178–187.
29. Jambor, J.L. Nomenclature of the Alunite Supergroup. *Can. Mineral.* **1999**, *37*, 1323–1341.
30. Jambor, J.L. Nomenclature of the Alunite Supergroup: Reply. *Can. Mineral.* **2000**, *38*, 1298–1303. [\[CrossRef\]](#)
31. Scott, K.M. Nomenclature of the Alunite Supergroup: Discussion. *Can. Mineral.* **2000**, *38*, 1295–1297. [\[CrossRef\]](#)
32. Mills, S.J.; Hatert, F.; Nickel, E.H.; Ferraris, G. The Standardisation of Mineral Group Hierarchies: Application to Recent Nomenclature Proposals. *Eur. J. Mineral.* **2009**, *21*, 1073–1080. [\[CrossRef\]](#)
33. Tikhomirov, P.L.; Akinin, V.V.; Ispolatov, V.O.; Alexander, P.; Cherepanova, I.Y.; Zagoskin, V.V. The Okhotsk-Chukotka Volcanic Belt: Age of Its Northern Part According to New Ar-Ar and U-Pb Geochronological Data. *Stratigr. Geol. Correl.* **2006**, *14*, 524–537. [\[CrossRef\]](#)
34. Lesnyak, D.V.; Ananyev, Y.S.; Gavrilov, R.Y. Structural, Geophysical and Geochemical Criteria for Epithermal High-Sulfidation Gold Mineralization on the Example of Svetloe Ore Field (Khabarovskiy Kray). *Bull. Tomsk Polytech. Univ. Geo Assets Eng.* **2022**, *333*, 60–72.
35. Moore, D.M.; Reynolds, R.C., Jr. *Diffraction and the Identification and Analysis of Clay Minerals*; Oxford University Press: Oxford, UK, 1997.
36. Bish, D.L.; Post, J.E. Quantitative Mineralogical Analysis Using the Rietveld Fullpattern Fitting Method. *Am. Mineral.* **1993**, *78*, 932–940.
37. Taylor, J.C. Computer Programs for Standardless Quantitative Analysis of Minerals Using the Full Powder Diffraction Profile. *Powder Diffr.* **1991**, *6*, 2–9. [\[CrossRef\]](#)
38. Steele-MacInnis, M.; Lecumberri-Sanchez, P.; Bodnar, R.J. HokieFlinCs_H₂O-NaCl: A Microsoft Excel Spreadsheet for Interpreting Microthermometric Data from Fluid Inclusions Based on the PVTX Properties of H₂O-NaCl. *Comput. Geosci.* **2012**, *49*, 334–337. [\[CrossRef\]](#)
39. Staude, S.; Mordhorst, T.; Neumann, R.; Prebeck, W.; Markl, G. Compositional Variation of the Tennantite–Tetrahedrite Solid-Solution Series in the Schwarzwald Ore District (SW Germany): The Role of Mineralization Processes and Fluid Source. *Mineral. Mag.* **2010**, *74*, 309–339. [\[CrossRef\]](#)
40. Arlt, T.; Diamond, L.W. Composition of Tetrahedrite-Tennantite and ‘Schwazite’ in the Schwaz Silver Mines, North Tyrol, Austria. *Mineral. Mag.* **1998**, *62*, 801–820. [\[CrossRef\]](#)
41. Krismer, M.; Vavtar, F.; Tropper, P.; Kaindl, R.; Sartory, B. The Chemical Composition of Tetrahedrite-Tennantite Ores from the Prehistoric and Historic Schwaz and Brixlegg Mining Areas (North Tyrol, Austria). *Eur. J. Mineral.* **2011**, *23*, 925–936. [\[CrossRef\]](#)
42. Lyubimtseva, N.G.; Bortnikov, N.S.; Borisovsky, S.E. Coexisting Bournonite–Seligmannite and Tennantite–Tetrahedrite Solid Solutions of the Darasun Gold Deposit, Eastern Transbaikalia, Russia: Estimation of the Mineral Formation Temperature. *Geol. Ore Depos.* **2019**, *61*, 274–291. [\[CrossRef\]](#)
43. Keim, M.F.; Walter, B.F.; Neumann, U.; Kreissl, S.; Bayerl, R.; Markl, G. Polyphase Enrichment and Redistribution Processes in Silver-Rich Mineral Associations of the Hydrothermal Fluorite-Barite-(Ag-Cu) Clara Deposit, SW Germany. *Miner. Depos.* **2019**, *54*, 155–174. [\[CrossRef\]](#)
44. Hu, Y.; Ye, L.; Li, Z.; Huang, Z.; Zhang, J. Genesis of Fahlore in the Tianbaoshan Lead–Zinc Deposit, Sichuan Province, China: A Scanning Electron Microscopy–Energy Dispersive Spectroscopy Study. *Acta Geochim.* **2018**, *37*, 842–853. [\[CrossRef\]](#)
45. Repstock, A.; Voudouris, P.; Zeug, M.; Melfos, V.; Zhai, M.; Li, H.; Kartal, T.; Matuszczak, J. Chemical Composition and Varieties of Fahlore-Group Minerals from Oligocene Mineralization in the Rhodope Area, Southern Bulgaria and Northern Greece. *Mineral. Petrol.* **2016**, *110*, 103–123. [\[CrossRef\]](#)
46. Lyubimtseva, N.G.; Bortnikov, N.S.; Borisovsky, S.E.; Prokofiev, V.Y.; Vikent'eva, O.V. Fahlore and Sphalerite from the Darasun Gold Deposit in the Eastern Transbaikal Region, Russia: I. Mineral Assemblages and Intergrowths, Chemical Composition, and Its Evolution. *Geol. Ore Depos.* **2018**, *60*, 93–120. [\[CrossRef\]](#)
47. Lyubimtseva, N.G.; Bortnikov, N.S.; Borisovsky, S.E.; Vikent'eva, O.V.; Prokofiev, V.Y. Coupled Dissolution–Precipitation Reactions of Tennantite–Tetrahedrite Minerals in the Darasun Gold Deposit (Eastern Transbaikalia, Russia). *Geol. Ore Depos.* **2019**, *61*, 530–548. [\[CrossRef\]](#)
48. Voudouris, P.C.; Melfos, V.; Spry, P.G.; Kartal, T.; Schleicher, H.; Moritz, R.; Orтели, M. The Pagoni Rachi/Kirki Cu-Mo±Re±Au Deposit, Northern Greece: Mineralogical and Fluid Inclusion Constraints on the Evolution of a Telescoped Porphyry-Epithermal System. *Can. Mineral.* **2013**, *51*, 253–284. [\[CrossRef\]](#)

49. Plotinskaya, O.Y.; Kovalenker, V.A.; Rusinov, V.L.; Seltmann, R. Oscillatory Zoning in Goldfieldite from Epithermal Gold Deposits. *Dokl. Earth Sci.* **2005**, *403*, 799–802.
50. Tardani, D.; Reich, M.; Deditius, A.P.; Chrysosoulis, S.; Sánchez-Alfaro, P.; Wrage, J.; Roberts, M.P. Copper–Arsenic Decoupling in an Active Geothermal System: A Link between Pyrite and Fluid Composition. *Geochim. Cosmochim. Acta* **2017**, *204*, 179–204. [\[CrossRef\]](#)
51. Repstock, A.; Voudouris, P.; Kolitsch, U. New Occurrences of Watanabeite, Colusite, “Arsenosulvanite” and “Cu-Excess” Tetrahedrite-Tennantite at the Pef Ka High-Sulfidation Epithermal Deposit, Northeastern Greece. *Neues Jahrb. Mineral. Abh.* **2015**, *192*, 135–149. [\[CrossRef\]](#)
52. Dill, H.G. The Geology of Aluminum Phosphate and Sulphates of the Alunite Group Minerals: A Review. *Earth Sci. Rev.* **2001**, *53*, 35–93. [\[CrossRef\]](#)
53. Yanchenko, O.M.; Timkin, T.V.; Voroshilov, V.G.; Yakich, T.Y.; Mansour, Z. Nature of Phosphate Distribution within the Golden Weathering Crusts of the Tomsk Region. *Bull. Tomsk Polytech. Univ. Geo Assets Eng.* **2021**, *332*, 74–91. [\[CrossRef\]](#)
54. Brimhall, G.H.; Ghiorso, M.S. Origin and Ore-Forming Consequences of the Advanced Argillic Alteration Process in Hydrogene Environments by Magmatic Gas Contamination of Meteoric Fluids. *Econ. Geol.* **1983**, *78*, 73–90. [\[CrossRef\]](#)
55. Stoffregen, R. Genesis of Acid-Sulfate Alteration and Au-Cu-Ag Mineralization at Summitville, Colorado. *Econ. Geol.* **1987**, *82*, 1575–1591. [\[CrossRef\]](#)
56. Aoki, M.; Comsti, E.; Lazo, F.; Matsuhisa, Y. Advanced Argillic Alteration and Geochemistry of Alunite in an Evolving Hydrothermal System at Baguio, Northern Luzon, Phillipines. *Resour. Geol.* **1993**, *43*, 155–164.
57. Watanabe, Y.; Hedenquist, J. Mineralogical and Stable Isotope Zonation at the Surface over the El Salvador Porphyry Cu Deposit, Chile. *Econ. Geol.* **2001**, *96*, 1775–1797. [\[CrossRef\]](#)
58. Stoffregen, R.E.; Alpers, C.N.; States, U.; Survey, G.; Bypass, Y. Woodhouseite and Svanbergite in Hydrothermal Ore Deposits: Products of Apatite Destruction during Advanced Argillic Alteration. *Can. Mineral.* **1987**, *25*, 201–211.
59. Voudouris, P.C. Conditions of Formation of the Mavrokoryfi High-Sulfidation Epithermal Cu-Ag-Au-Te Mineralization (Petrota Graben, NE Greece). *Mineral. Petrol.* **2011**, *101*, 97–113. [\[CrossRef\]](#)
60. Voudouris, P.C.; Melfos, V.; Spry, P.G.; Moritz, R.; Papavassiliou, C.; Falalakis, G. Mineralogy and Geochemical Environment of Formation of the Perama Hill High-Sulfidation Epithermal Au-Ag-Te-Se Deposit, Petrota Graben, NE Greece. *Mineral. Petrol.* **2011**, *103*, 79–100. [\[CrossRef\]](#)
61. Naderi, M.; Modabberi, S.; Tarantola, A.; Haroni, H.A. Mineralogical and Geochemical Constraints on the Origin of Alunite and APS Minerals from Advanced Argillic Alteration Systems: A Case Study from Kuh-e-Lakht Au-Ag-Cu Mineralization, NE Isfahan, Iran. *J. Geochem. Explor.* **2024**, *262*, 107467. [\[CrossRef\]](#)
62. Wang, L.; Qin, K.Z.; Song, G.X.; Li, G.M. A Review of Intermediate Sulfidation Epithermal Deposits and Subclassification. *Ore Geol. Rev.* **2019**, *107*, 434–456. [\[CrossRef\]](#)
63. Shapovalova, M.; Shaparenko, E.; Tolstykh, N.D. Geochemistry and Fluid Inclusion of Epithermal Gold-Silver Deposits in Kamchatka, Russia. *Minerals* **2025**, *15*, 2. [\[CrossRef\]](#)
64. Bodnar, R.J.; Lecumberri-Sanchez, P.; Moncada, D.; Steele-MacInnis, M. *Fluid Inclusions in Hydrothermal Ore Deposits*, 2nd ed.; Elsevier Ltd.: Amsterdam, The Netherlands, 2013; Volume 13, ISBN 9780080983004.
65. Keith, M.; Smith, D.J.; Jenkin, G.R.J.; Holwell, D.A. Global Se and Te Systematics in Hydrothermal Pyrite from Different Ore Deposits: A Review. *Appl. Earth Sci.* **2017**, *126*, 70–71. [\[CrossRef\]](#)
66. Keith, M.; Börner, F.; Smith, D.J.; Barry, T.L.; Neumann, T.; Klemd, R. Epithermal Pyrite as Target for Tellurium Exploration in Vatukoula, Fiji. In Proceedings of the DMG Virtual Poster Session 2020, Virtual, 30 November–3 December 2020; 2020; pp. 2–3.
67. Timkin, T.; Voroshilov, V.; Askanakova, O.; Cherkasova, T.; Chernyshov, A.; Korotchenko, T. Estimating Gold-Ore Mineralization Potential within Topolninsk Ore Field (Gorny Altai). In Proceedings of the IOP Conference Series: Earth and Environmental Science, XIX International Scientific Symposium in Honor of Academician M.A. Usov “Problems of Geology and Subsurface Development”, Tomsk, Russia, 6–10 April 2015.
68. Cherkasova, T.; Kucherenko, I.; Abramova, R. Rear Polymineral Zone of Near-Veined Metasomatic Aureole in Mesothermal Zun-Holba Gold Deposit (Eastern Sayan). In Proceedings of the IOP Conference Series: Earth and Environmental Science, XIX International Scientific Symposium in Honor of Academician M.A. Usov “Problems of Geology and Subsurface Development”, Tomsk, Russia, 6–10 April 2015.

Disclaimer/Publisher’s Note: The statements, opinions and data contained in all publications are solely those of the individual author(s) and contributor(s) and not of MDPI and/or the editor(s). MDPI and/or the editor(s) disclaim responsibility for any injury to people or property resulting from any ideas, methods, instructions or products referred to in the content.